INAUGURAL - DISSERTATION

ZUR

ERLANGUNG DER DOKTORWÜRDE

DER

NATURWISSENSCHAFTLICH-MATHEMATISCHEN

GESAMTFAKULTÄT

DER

RUPRECHT-KARLS-UNIVERSITÄT

HEIDELBERG

vorgelegt von

Diplom-Mathematiker Dietmar Volz

aus Baden-Baden

Modeling of light propagation in skin, and
an application to noninvasive diagnostics

Gutachter: Prof. Dr. Dr. h.c. mult. Willi Jäger
Prof. Dr. Dr. h.c. Hans-Georg Bock

Tag der mündlichen Prüfung:

Preface

Diabetics would greatly benefit from a device capable of providing continuous noninvasive monitoring of their blood glucose levels. At present, diabetics rely on pricking their finger to obtain a blood sample which in turn is placed upon a test strip. Life long finger pricking is often accompanied by chronic infections and pain during the lancets prick. Moreover, to significantly reduce longer-term secondary effects of diabetes such as retinopahy, nephropathy or neuropathy on the one hand and to reduce the risk of unnoticed suffering from hypoglycemia on the other hand a more frequent or even continuous monitoring of blood glucose swings is needed.

In the past decade several attempts have been made to measure the glucose content of blood in a more compliant fashion. These endeavors will gain importance in the near future. Already nowadays, diabetes ranges among the top civilization deseases, about 10% of all U.S. citizens are living with this diagnosis, European citizens will make up in the future.

Many techniques have been suggested for continuous monitoring of glucose, ranging from implanted electrochemical sensors to noninvasive optical methods. So far none of these methods have proven to be sensitive or specific enough for commercial use.

The method proposed in this thesis deals with an effect which is based upon changes of the light scattering coefficient in the upper dermal regions of skin induced by glucose dissolved in the interstitial fluid. We will focus on the identification of this coefficient in vivo. As we want to probe our tissue with decoherent light of a single wavelength in the near infrared regime, the physical process is properly described by the radiative transfer equation.

The modeling has to face the task of mapping a special measurement setting as well as spatial and temporal varying skin optical properties to a proper boundary value problem formulation for the radiative transfer equation and an effective solution of the inverse problem. As we will soon recognize, an effective solution of the forward and more urging of the inverse problem is necessarily based on approximations of the radiative transfer equation, especially the diffusion approximation will be treated in detail. Moreover we will have to excurse to data-driven approaches in order to overcome the limitations of modeling within partial differential equations which have been revealed to be obvious for this problem.

This thesis resulted from a cooperation between Boehringer Mannheim GmbH respectively their successor Roche diagnostics GmbH in Mannheim and the Interdiscplinary Center for Scientific Computing in Heidelberg. It is written in the sense of bringing together sophisticated mathematics with the complexity of an in vivo setting, and is thus completely problem oriented.

Contents

List of Figures

Introduction

Among other noninvasive monitoring techniques such as ultrasound and magnetic resonance imaging the use of light in the near infrared regime (NIR) leads to one of the least space consuming measurement settings known, resulting probe units are portable and easy to handle. In this regard, about 15 years ago an effect has been found that revealed a correlation between the light scattering coefficient (LSC) of upper skin tissue and its glucose content. Some time later, this effect was explained by the optical properties of interstitial fluid (ISF) which are changing under the soaking influence of glucose. Namely the LSC of skin tissue is dependent on the refractive index mismatch between the ISF and the cellular membranes, which can be proven quantitatively by Mie theory if we assume the tissue cells to be given by geometrical objects of simple shape (e.g. balls or cylinders) [6]. The LSC is therefore a macroscopic parameter, the correlation to the underlying microscopic cell membrane optical effects is assumed to be given. The correlation between glucose levels in the ISF and the LSC of skin, for the sake of brevity we will refer to it as the *glucose effect*, has been reproduced in skin tissue-simulating phantoms [37] and studies with volunteers for the in vivo setting [8].
In order to measure the scattering coefficient of upper skin, different possibilities to fix a probe unit onto skin are conceivable, such as light transmittance through the earlobe or reflectance measurements. In the latter case the light is usually radiated perpendicular into skin and an array of also perpendicular oriented detectors measure the backscattered photons. In this thesis we deal with a probe unit which consists of a single illuminating fiber and a dozen collecting fibers arranged for NIR reflectance measurements.
In the past, the problem of identifying the interesting scattering coefficient within the many other parameters that interfere with the measured signal has been approached by pure data driven methods, such as neural networks and by parameter estimation algorithms based on skin models to enter the radiative transfer equation (RTE). Particularly models based on the diffusion approximation of the RTE have been investigated in detail by several authors. Within this approximation, the appliance of a fresnel boundary condition on the top of skin to build a semi-infinite geometry has been asserted to be computationally cheap and accurate at source-detector distances a few mean free paths apart from the light source. This in turn is meaningful owing to the demand on portability of the probe and its data evaluation device on the one hand and the circumstance that we have to evaluate signals continuously i.e. several times a minute on the other hand.

Modeling in noninvasive diagnostics therefore has to face the problem of combining a small computation complexity and the ability of coping with skin optical parameters which vary spatially and temporaly on different scales as well as between individuals.

In this thesis we embark on the following strategy:
First, we introduce radiative transport theory outlining the Cauchy problem of radiative transport and related problems that have especially been developed in nuclear reactor theory. Next, we advance to the diffusion approximation of the RTE and will establish a layered skin model using the method of images, likewise borrowed from nuclear reactor theory. Progress and restrictions will be discussed especially concerning models for small layers (e.g. epidermal), fourier space models, and the use of a gaussian convolution kernel in order to model the scattering inside the bottom layer of a two-layer model. Furthermore, we will propose a heuristics to model the light trait in the vicinity of a directed light source within a proper class of functions, a relation to a fundamental solution of a feasable diffusion equation and first results for in vivo data.
Using the law of Lambert-Beer, we will derive an algorithm to separate absorption changes, and present some results for in vivo data. In the last chapter we will have to excurse to data-driven approaches in order to cope e.g. with drift artefacts that pollute to a great extent our in vivo experiments. A new higher-order method, namely independent component analysis (ICA) will be proposed and an implementation issued by the neural network research centre at Helsinki University of Technology will be applied to in vivo data. Combining a model-based approach and the ICA approach, we will outline a hybrid method to simultaneously successfully eliminate absorption artefacts, and an existing drift artefact.

Chapter 1

Medium, Probe Unit

1.1 Skin Tissue: Anatomy, Physiology

We will review the anatomical and physiological properties of skin, provided they affect skin optical properties and changes thereof. First, we have to speak of skin as a layered medium, namely we can distinguish three different types of tissue which are called the *epidermis*, the *dermis* and the *subcutis layer*. The epidermal layer could be further distinguished into the *stratum corneum* and the *stratum basale*. The following picture shows the anatomical structure of skin including specifications and several substructures like hair, sweat glands and first of all the capillary loops at the upper dermis:

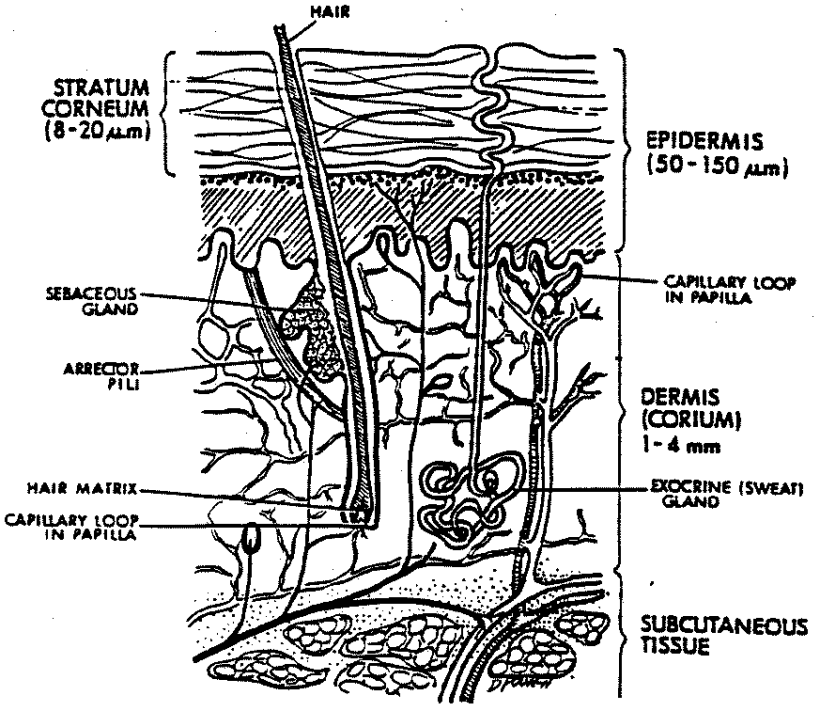

Figure 1.1: Skin tissue in sectional view, (*Source:* Roche [48]).

Figure 1.2 shows a three-dimensional view of an in vivo scan obtained by *optical coherence tomography*. The stack of two-dimensional sectional slices was merged to a three-dimensional picture by an algorithm developed by C. Dartu at the IWR Heidelberg.

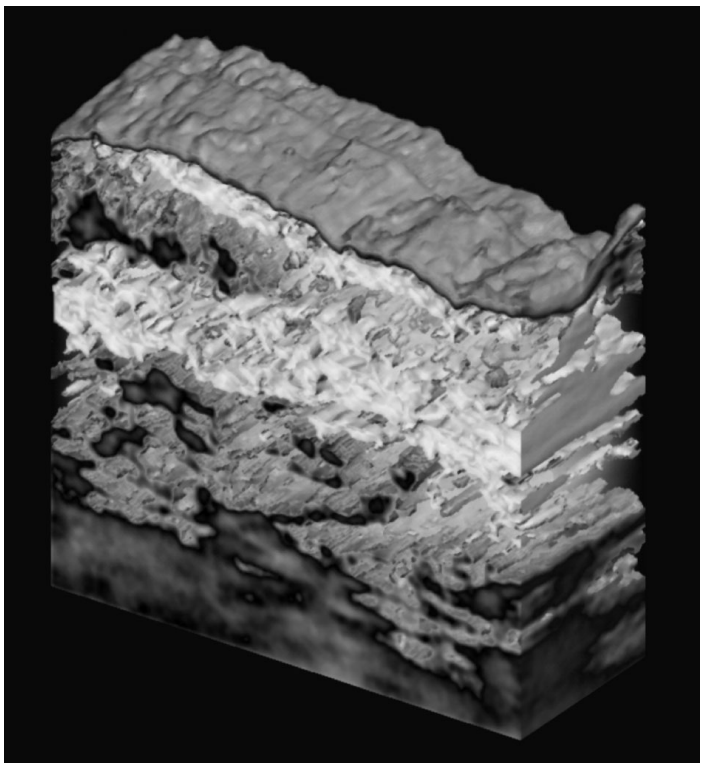

Figure 1.2: Skin tissue in three dimensions, about 500μm deep.

The capillary loops are of special importance because they accomplish the exchange of substances produced or consumed by tissue cells (glucose, oxygen, carbon dioxide etc.). The exchange of such substances through capillary walls is maintained by diffusion along the concentration gradient which in turn causes a time lag between concentration changes of blood constituents and their counterparts in ISF. Although the statements vary to a great extent, it turns out that at increasing blood glucose concentrations the time delay is about 5min and at decreasing blood glucose concentrations it is about 8min [48]. The time delay varies significantly intra- and inter-individually and may depend on blood flow, tissue structure, the sensors implantation site, the actual tissue metabolic requirements etc. An ISF glucose signal corresponds in some sense to a regularized version of the respective blood glucose signal: sharp glucose peaks provoked e.g. by glucose infusion are mapped to smooth ISF glucose swings. This fact is of importance if we want to calibrate a noninvasively measured ISF glucose signal by blood glucose measurements. Figure 1.3 illustrates the difference under the assumption of a linear correlation between the scattering coeffitient μ_s' and ISF glucose. The physiological characteristics of interest are mainly governed by changes in blood flow, blood consistency, blood volume and water content of skin. Physical changes of interest

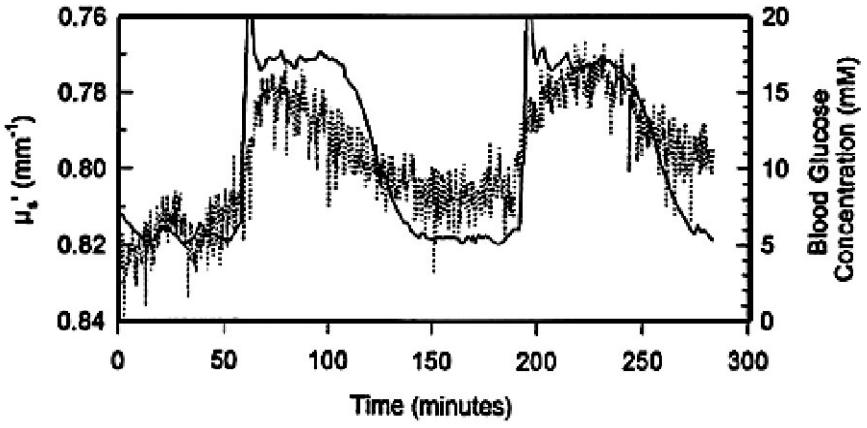

Figure 1.3: Glucose clamps & glucose swings (noisy), (*Source:* Roche [8]).

concern temperature variations and mechanical impact.

1.2 Skin Optical Parameters

As we are interested in the modeling of skin structure within radiative tranport theory we have to map the anatomical and physiological facts given above to skin optical parameters in a meaningful way. In the following we will distinguish between *absorption* and *scattering* properties of the influencing factors as they ensue for NIR or visible light. Additionally, each layer change defines a certain boundary involving a proper boundary condition. In particular we get the following schedule:

i. Epidermis
The main absorbing constituents are water and the skin pigment melanin. Due to its small thickness $(50 - 150\mu\text{m})$ the specific absorption is small compared to the total absorption inside skin. The specific scattering is also small with a strong forward orientation. The refractive index ratio between stratum corneum and stratum basale is about $n_{rel} \simeq 1.51/1.34$, [52].
Because the epidermis has no blood supply there is no direct absorption change due to blood induced physiological variations. But the epidermis is influenced by temperature changes and changes of water content, which has a crucial impact on scattering properties as well as on the boundary structure.

ii. Dermis
The main absorption inside dermis in the range of 600nm to 900nm is caused by haemoglobin absorption. We distinguish between oxygenated and deoxygenated haemoglobin whose ab-

sorption spectra are discussed in the excursus below.
As in the introduction stated, the glucose effect has its roots in the difference between the refractive index of ISF and cell membranes, where the former is altered. More specific: the refractive indices are $n = 1.35$ for the ISF and $n \simeq 1.38$ for the membranes [27]. An increase of glucose in the ISF yields an increase of the refractive index of the ISF and thus decreases the difference to the index of the membranes with the consequence that the scattering coefficient decreases: the glucose effect is anticorrelated to glucose changes.
We don't want to forget the collagen fibers which constitute about 20% of the dermis volume. They make up the so called *Langer lines*, which give skin a permanent tension. It has recently been found that they also give light a preferred scattering direction: light scattering inside dermis is greater perpendicular to those lines than along them [23] [45].
Due to the strong blood circulation especially at the upper dermal regions we can assume isothermal conditions except for the reason of physiologically induced blood circulation changes.

Both, epidermal as well as dermal tissue are scatter-dominated media. Specific values for absorption and scattering coefficients will be given in the next chapter.

iii. Subcutis
The subcutis consists in the main part of fatty connective tissue cells. Both, the scattering coefficient and the absorption coefficient are smaller than inside the dermis.

1.2.1 Excursus: Measuring Blood Oxygenation

We excurse to a method of noninvasive blood constituent measurement which utilizes the virtue of having specific absorption spectra. As can be seen in figure 1.4 there is a clear difference in the absorption spectra of oxygenated to deoxygenated haemoglobin except in one point. At this *isosbestic point* at $\lambda_i = 805$nm the extinction coefficients of haemoglobin and oxyhaemoglobin coincide. The extinction is given by the law of Lambert-Beer:

$$E = \epsilon_\lambda \cdot c \cdot d \quad . \tag{1.1}$$

The extinction E is a product of the pathlength d , the extinction coefficient ϵ_λ and the concentration c . It is now possible to track temporal variations in blood oxygenation by building the quotient $E_\lambda / E_{\lambda_i}$. If we assume that the optical path lengths of photons at both wavelengths are almost equal, we get a measure which correlates to the oxygenation change [36].
Blood oxygenation is one of the few well understood and controllable physiological parameters. Unfortunately the situation for glucose is much less specific: The absorption coefficient for glucose in the diagnostic window lies between 10^{-3} and 10^{-2}cm^{-1} . In the visible and NIR range, absorption is thus clearly dominated by other blood constituents and consequently there is no possibility to track glucose changes by utilization of absorption

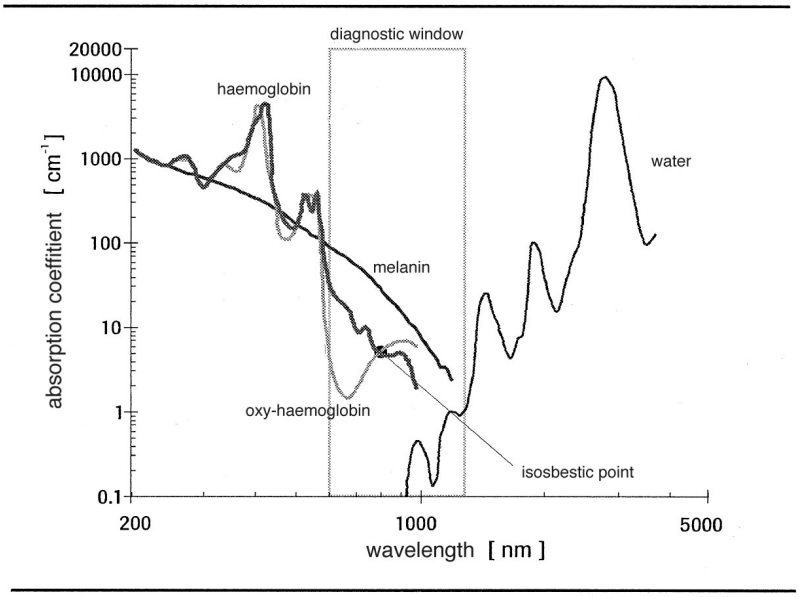

Figure 1.4: Absorption spectra of different blood constituents, (*Source:* Klötzer [36]).

spectra only.

Summary and Annotations

Skin is organized in layers which are heterogeneous in themselves on different scales. They vary in tissue compartimentation, skin appendages, organization and distribution of blood vessels, regional differences in tissue structure etc.

Variations of blood volume, blood flow and haemoglobin oxygenation are mostly responsible for absorption changes in skin tissue thus interfering with noninvasive ISF glucose monitoring.

It is virtually impossible to eliminate the influence of most of the interfering processes on glucose determination by keeping them constant, at least under normal life conditions since the underlying regulation mechanisms are very complex, strongly linked to each other, and essential for maintaining the viability of the human body. Therefore interfering processes have to be eliminated by algorithms applied to the devices signal.

1.3 The Probe Unit

The probe used for the measurements consists of a linear array of optical fibers with a core diameter of 200μm. There are two types of fibers, namely one illuminating fiber (source) and a dozen collecting fibers at distances ranging from 0.8 to 10mm from the illuminating point. The source light is switchable between different single wavelengths in the NIR range and power stabilized in direct current (DC) mode. Both, the illuminating fiber and the collecting fibers are oriented perpendicular to the skin surface. The source light has the characteristics of a pencil beam and is thus anisotropic. The paths of the photons arriving at the detector fibers are characterized by multiple reflections and backscattering. Summarizing, we speak of spatially-resolved reflectance measurements in DC mode.
A crucial point in noninvasive measurements is the connection of the probe to the skin surface. We assume that the connection prevents the probe from slipping on the skin and that the interface material provides stable optical conditions between the probe and the skin surface. Especially the interface material has almost no scattering and almost no absorption. Figure 1.5 shows a sectional view of the probe in original size and the decreasing reflectance dependent on the source-detector distance. Contrary to the suggestion of figure 1.5, the

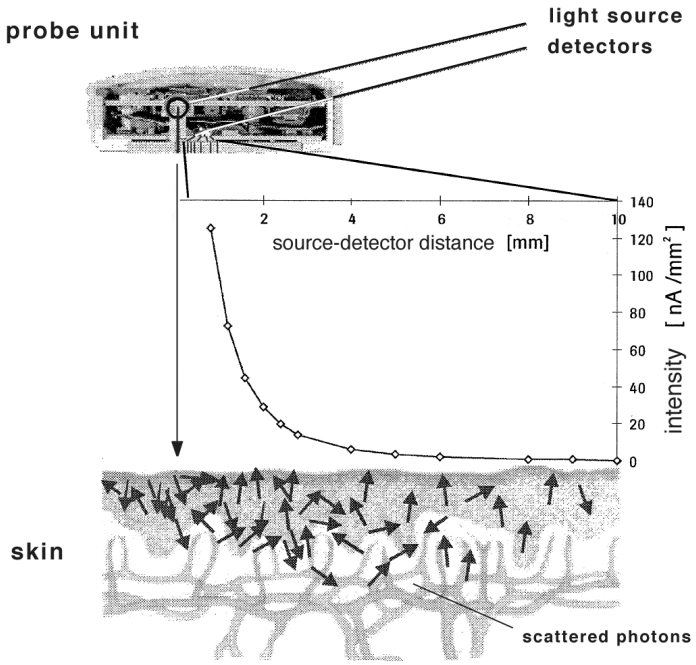

Figure 1.5: The NIT 1.37 probe unit, scattered photons in upper skin and a characteristic reflection profile, (*Source:* Roche [36]).

distance between the skin surface and the probe surface is exclusively dependent on the thickness of the interface material which amounts to about several tenth of a millimeter. However, all modeling proposed in this thesis assumes the fibers to be placed directly above the epidermis i.e. the top boundary of skin.

Chapter 2

Modeling within Radiative Transport Theory

2.1 Analysis of the RTE

We start our considerations with an equation that describes the dynamics of light in a scatter-dominated medium. In the following, we assume that the phase relations of photons vanish after a few scattering events. Accordingly, the Maxwell equations which are convenient to describe the wave character of light can be replaced by an equation that describes gas dynamics which in turn is comparable in a very high accuracy to photon dynamics [31]. If we assume the unique velocity of light c, we get in the monochromatic case the *radiative transfer equation* (RTE) which is a linear equation in the NIR regime [10]:

$$\frac{1}{c}\frac{\partial u}{\partial t} + \theta \cdot \nabla u(x,\theta,t) + \mu_t(x)u(x,\theta,t) = \mu_s(x)\int_{S^2} \eta(\theta\cdot\theta')u(x,\theta',t)d\theta' + q(x,\theta,t) \quad , \quad (2.1)$$

for $(x,\theta,t) \in I\!R^3 \times S^2 \times I\!R^+$,

with the angle-, space-, and time-dependent radiation intensity u, and source q. In skin tissue the *attenuation coefficient* $\mu_t(x) = \mu_s(x) + \mu_a(x)$ almost equals the *scatter coefficient* $\mu_s \sim 15$ which is about 1000 times bigger than the *absorption coefficient* $\mu_a \sim 0.01$. The integral kernel η known as *phase function* is normalized:

$$\int_{S^2} \eta(\theta,\theta')d\theta' = 1 \quad ,$$

and fulfills the symmetry conditions:

$$\begin{aligned} \eta(\theta,\theta') &= \eta(-\theta,-\theta') \quad , \\ \eta(\theta',\theta) &= \eta(\theta,\theta') \quad . \end{aligned}$$

Two possibilities of fulfilling these conditions are given by:

$$\eta(\theta,\theta') = P(\cos\alpha) = \begin{cases} \text{const.} & \text{isotropic scattering,} \\ \frac{1}{4\pi}\frac{1-g^2}{(1+g^2-2g\cos\alpha)^{3/2}} & \text{Henyey-Greenstein scattering.} \end{cases}$$

To go more into detail, the phase function P is expanded into spherical harmonics:

$$P(\cos\alpha) = \frac{1}{4\pi}\sum_{k=0}^{N}(2k+1)m_k L_k(\cos\alpha) \quad , \tag{2.2}$$

where the L_k's are the Legendre polynomials of the order k. Following the Henyey-Greenstein interpretation of anisotropic scattering, the components m_k are expressed by constant exponentials $m_k = g^k$ and $N = 2$. The parameter g is called the *anisotropy parameter*. It is defined as the average cosine of the scattering angle α [54]:

$$g \;:=\; \frac{\int_{S^2}(\theta\cdot\theta')P(\cos\alpha)d\theta'}{\int_{S^2}P(\cos\alpha)d\theta'} \quad , \quad \alpha = \angle(\theta,\theta') \quad .$$

The Henyey-Greenstein phase function is commonly used in tissue optics and has been proven to fit experimental data for a wide range of tissue types, where $g \simeq 0.9$ which stands for a strong forward direction of scattering [50] [54].

2.1.1 The Cauchy Problem of Radiative Transport

We will sketch one possibility of putting up a boundary structure and initial values for equation 2.1 to yield the *Cauchy problem* of the transport equation. We will outline some existence and uniqueness results concerning this problem and refer to the book of R. Dautray and J. L. Lions [15] for further details and proofs.
The Cauchy problem of the time-dependent RTE is formulated as follows:

Problem 2.1 *Find a solution* $u(x,\theta,t)$ *for equation 2.1, and* $(x,\theta,t) \in I\!R^3 \times S^2 \times]0,\tau[$,

with the initial condition $u(x,\theta,0) = u_0(x,\theta)$ *in* $V \times \Theta \subset I\!R^3 \times S^2$, V *compact* ,
and the boundary condition $u(x,\theta,t) = b(x,\theta,t)$ *on* $\Gamma_- = \{(x,\theta) \in \partial V \times \Theta; n\cdot\theta < 0\}$,

where n *denotes the outward normal to* ∂V *at* x.

Remark 2.1 *We mention two special types of Cauchy problems that have been considered in the past especially to model the neutron dynamics inside nuclear reactors. The one problem is called the* reactor problem *which is characterized by the lack of sources and reflecting boundaries (no neutrons come from outside into the reactor), V is hereby relative-compact, open and convex in $\mathbb{R}^3$. The other problem is called the* scattering problem *and is defined on whole $\mathbb{R}^3$. Both problems are given initial values u_0. The interested reader is e.g referred to the work done by Choulli & Stefanov [11]. They utilized the scattering problem to investigate tissue media by extension of the restricted scattering area V by a vacuum area $\mathbb{R}^3 \setminus V$ so that there are no interactions of the photons inside $\mathbb{R}^3 \setminus V$ with the surrounding area. We stress that the results obtained in nuclear physics are hardly transferable to the much more complex case of living tissue.*

To treat the general Cauchy problem, we first define the function space $L^p(V \times \Theta), \quad p \in [1, \infty[$ to be the space of all functions f which are measurable in respect to the product measure $dxd\theta$ such that

$$\|f\|_{L^p(V\times\Theta)} := \left(\int_{V\times\Theta} |f(x,\theta)|^p dxd\theta \right)^{1/p} < \infty \quad .$$

We want to search for solutions in the spaces $L^p(V \times \Theta)$. A kind of natural choice would be to take the $L^p(V \times \Theta)$ with $p = 1$ due to the interpretation of the total current of photons $N(t)$ at time t in configuration space:

$$\|u\|_{L^1(V\times\Theta)} = \int_{V\times\Theta} u(x,\theta,t) dxd\theta =: N(t) < \infty \quad .$$

In analogy to the $L^p(V \times \Theta)$ spaces, we define the $L^p(V \times \Theta \times]0, \tau[)$ spaces and the sobolev spaces $W^p(V \times \Theta \times]0, \tau[)$ to be those spaces of functions f such that f and its distributional derivatives $D^s f$ of order $|s| = \sum_{j=1}^{n} |s_j| \leq k$ all belong to $L^p(V \times \Theta \times]0, \tau[)$. W^p is a normed linear space, for further details on those spaces see e.g. [58]. We are now able to formulate theorems of existence and uniqueness for problem 2.1 in the homogeneous case $b = 0$.

Theorem 2.1 *For*

$$a(x,\theta) \in L^\infty(V \times \Theta) \quad , \quad a \geq 0$$

and

$$\begin{aligned} \int_{S^2} \eta(x,\theta',\theta) d\mu(\theta) &\leq C_1 \qquad \forall (x,\theta') \in V \times \Theta \\ \int_{S^2} \eta(x,\theta',\theta) d\mu(\theta') &\leq C_2 \qquad \forall (x,\theta) \in V \times \Theta \end{aligned}$$

with positive constants C_1, C_2 , and

$$\begin{aligned} q &\in L^p(V \times \Theta \times]0, \tau[) \quad , \qquad p \in [1, \infty[\quad , \\ u_0 &\in L^p(V \times \Theta) \quad , \end{aligned}$$

problem 2.1 with $b = 0$ has a unique solution in W^p .

Theorem 2.2 *If further the following consistency condition is fulfilled:*

$$\begin{aligned} \theta \cdot \nabla u_0 &\in L^p(V \times \Theta) \quad , \qquad u_0|_{\Gamma_-} = 0 \\ q &\in C^1([0,\tau]; L^p(V \times \Theta)) \quad , \end{aligned}$$

then u is a strong solution of 2.1; it satisfies:

$$\begin{aligned} u &\in C^1([0,\tau]; L^p(V \times \Theta)) \quad , \\ \theta \cdot \nabla u &\in C^0([0,\tau]; L^p(V \times \Theta)) \quad , \\ u(t)|_{\Gamma_-} &= 0 \quad , \quad \forall t \in [0,\tau] \quad . \end{aligned}$$

If $q \geq 0$, then $u_0 \geq 0$ implies $u \geq 0$.

In the case of an inhomogeneous boundary condition $b \in L^p \neq 0$ we have an existence and uniqueness result in a weak sense as stated in [15] and also the positivity result: If b, u_0 and q are positive then the solution u of the inhomogeneous problem is also positive.

Remark 2.2 *The previous theorems inclose the fact that transport problems as opposed to related diffusion problems do not have a regularizing effect to their solutions. Both in the homogeneous and the inhomogeneous case u can be discontinuous even for $u_0 \in C^\infty$, especially if the domain has 'holes' [15].*

Analoguous existence and uniqueness results are given for the stationary RTE as can be seen in the references [9] [15].

2.1.2 The Inverse Scattering Problem

If we look at transport equation 2.1 and assume that the scattering integral is identical to zero, we are in a regime were the attenuation coefficient $\mu_t(x)$ is uniquely determined by boundary data [1]. The algorithm which performs this inversion is called an *inverse Radon transform* and all reconstruction techniques in X-ray tomography are based on this transformation. It is now an interesting question as to what rate it is possible to reduce the energy of X-ray photons thus leading a scattering integral $\neq 0$ until in the NIR regime at least parts of the medium are scatter-dominated. Choulli & Stefanov [11] as well as Antyufeev & Bondarenko [7] have proven existence and uniqueness results of an inverse problem to equation 2.1 in the case of given boundary data, i.e. the possibility of reconstructing the attenuation coefficient under certain conditions on $\mu_t(x)$ and η and -unfortunately- in the case of weak scattering. This is due to the fact that one applies a Radon transform to the singular structures of the solutions and therefore to the maximally once scattered photons: E. W. Larsen

[1] within a class of appropriate regularizations [42]

has proven that such singular structures exist in $L^1(V \times \Theta)$ and that those terms are due to unscattered or maximally once scattered photons, the portion of all other photons has been proven to be describable by regular integrals [38]. But in the scatter-dominated case it is impossible to measure unscattered or once scattered photons separately from other photons: the probability for a photon to get through tissue of the thickness 10mm unscattered is about $\exp(-100)$. Existence and uniqueness results are obsolete a few mean free paths (mfp) apart from the light source in the diffusion regime as we will see in chapter 4. Therefore, classical reconstruction techniques are not applicable in scatter-dominated media. Correction of scattering artefacts as well as the identification of a scattering-dependent parameter will depend on the accuracy of a model used for parameter estimation.

2.2 Discretizations of the RTE

2.2.1 Monte-Carlo Simulation

An easy to handle and very intuitive way to discretize transport problems is the *Monte-Carlo method* which in opposition to the demanding and usually sophisticated PDE solvers based on finite-differences is mainly used when only qualitative influences of e.g. measurement settings on the reflectance profile have to be investigated. Contrary to finite-difference methods there is no error control depending on the discretizing demands of local structures of the medium, the error is only asymptotically controllable with unknown constants, i.e. the quality of the simulation depends on the number of photon runs which are usually in the range of $10^7 - 10^8$. Due to the very slow convergence, the computation costs are respectively high and amount from several hours to days on a usual workstation. A very useful and often used implementation is the MCML code of Wang & Jacques [47] which is public domain and covers most of everydays demands on probe simulation, skin phantom specification as well as the verification of physiologically motivated skin optical effects in vivo, for examples we refer e.g. to [23] [32].

2.2.2 Finite-Difference Methods

For the sake of completeness we want to mention *finite-difference methods* and their most important representative the *finite-element methods*. Due to the utilization of the so-called *galerkin orthogonality*, the latter methods obtain optimal error control contrary to Monte-Carlo simulations.

Concerning a priori and a posteriori estimates for galerkin and petrov-galerkin methods as well as several acceleration schemes like crosswind diffusion, streamline diffusion and the whole endeavors made in adaptive grid refinement we want to mention the research team of R. Rannacher et al. at Heidelberg University and some of their publications [18] [31] for

further investigations. An overview of the methods has been given e.g. by the book of Lewis & Miller,Jr. [40].

2.3 Evaluation

The attempts to solve the RTE in the case of scatter-dominated media leads to computation costs which are preferentially settled on large non-portable computing devices. Especially research teams who have focussed on the development of NIR imaging algorithms which yield a spatially resolved three-dimensional parameter space (usually the attenuation coefficient) are subject to this circumstance. We mention the research teams of A. Hielscher at SUNY downstate medical center, Brooklyn, and of S. Arridge at King's Colledge, London. Both teams raise the claim of identifying the attenuation coefficient within NIR datasets in three dimensions. They confirm that in most cases it is still impossible at the moment to even state whether those endeavors for all kind of tissues will succeed [4].
In general, theoretical motivated benchmarking as well as the formulation of existence and uniqueness results for complex geometries remain open. At the moment it seems that the search for some kind of "Radon transform for scattering media" will produce no results and most likely will never do, at least for scatter-dominated media.
Having this in mind, the strategy of solving an inverse boundary value problem for the RTE several times an hour on a portable device has to be thought over. Therefore in the following two chapters we try to handle the problem on the basis of an approximation.

Chapter 3

The Diffusion Approximation

The motivation to take the diffusion approximation of the RTE is due to the fact that skin is a scatter-dominated medium, and therefore the dynamics of photons a few mfp apart from a directed light source is describable by a diffusion process. On the basis of this approximation, multi-layer models will be formulated in order to meet skin optical properties. Due to the regularizing effect of diffusion processes, the solutions of those models all are in C^∞. We do not have to weaken the topology of our function spaces to Sobolev spaces. Additionally, a heuristics to treat the characteristics of light propagation in the vicinity of a directed light source will be proposed. The models are usually formulated in three space dimensions and time domain (DC mode if stated). We repeat the RTE of chapter 2 to write:

$$\frac{1}{c}\frac{\partial u}{\partial t} + \theta \cdot \nabla u(x,\theta,t) + \mu_t(x)u(x,\theta,t) = \mu_s(x)\int_{S^2} \eta(\theta\cdot\theta')u(x,\theta',t)d\theta' + q(x,\theta,t) \qquad (3.1)$$

for $(x,\theta,t) = (r,z,\theta,t) \in I\!R^2 \times I\!R \times S^2 \times I\!R^+$.

It is transformed to a continuity equation by integrating over all solid angles and using the definitions of the fluence rate Φ and the flux J:

$$\frac{1}{c}\frac{\partial \Phi(x,t)}{\partial t} + \nabla J(x,t) = -\mu_a \Phi(x,t) + Q(x,t) \quad , \qquad (3.2)$$

where

$$\Phi(x,t) = \int_{S^2} u(x,\theta,t)d\theta \quad , \qquad (3.3)$$

$$J(x,t) = \int_{S^2} \theta \cdot u(x,\theta,t)d\theta \quad , \qquad (3.4)$$

$$Q(x,t) = \int_{S^2} q(x,\theta,t)d\theta \quad .$$

If we assume Fick's diffusion law:

$$J(x,t) \;:=\; -\,D(x)\cdot\nabla\Phi(x,t) \quad ,$$

we arrive at the *diffusion approximation* of the RTE:

$$-\nabla\cdot D(x)\nabla\Phi(x,t)+\mu_a\Phi(x,t)+\frac{1}{c}\frac{\partial\Phi(x,t)}{\partial t}=Q(x,t) \quad , \quad (x,t)\in I\!R^3\times I\!R^+ \quad , \tag{3.5}$$

using the definitions:

$$Q(x,t) \qquad \text{isotropic source,} \tag{3.6}$$

$$D(x)=1/3(\mu_a(x)+\mu_s'(x)) \qquad \text{diffusion coefficient}^1, \tag{3.7}$$

$$\mu_s'(x)=(1-g)\mu_s(x) \qquad \text{reduced scattering coefficient} \quad . \tag{3.8}$$

$$\tag{3.9}$$

In the definition of the reduced scattering coefficient, the parameter g corresponds to the anisotropy parameter defined in chapter 2.
A solution of 3.1 also satisfies equation 3.5 if (see also [15]):

i. the light sources are isotropic,

ii. the solution is considered far from boundaries and far from zones where the medium parameters vary strongly, (3.10)

iii. the medium is scatter-dominated ($\mu_s >> \mu_a$).

Remark 3.1 *If condition iii holds, then for source-detector distances greater than two to three mfp a solution of equation 3.1 behaves as if assumption i would hold. In tissue media, we therefore assume that the characteristics of the light trait remains constant for distances greater than two to three mfp from the source.*

Exact estimates for the applicability of the diffusion approximation exist for very simple geometries only. In section 3.1.4 we will sketch a result given in [15] for the Cauchy problem. The extension to complex geometries of tissue optics is a subject of permanent -principally phenomenological- research. For comparisons to Monte-Carlo simulations see e.g. [49], and for comparisons to two-layer models see e.g. [1] [23].

[1]Some authors argue that $D(x) = 1/3\mu_s(x)$ is the right definition of the diffusion coefficient. For a contribution to the discussion see e.g. [3] [16]

3.1 Boundaries - The Semi-Infinte Medium

In the next step in skin modeling within the diffusion approximation we will map the layer structure of skin to a proper boundary setting. For simplicity, we assume that skin layers are connected by parallel oriented planes applying translationally invariant boundaries with a proper boundary condition. We begin our considerations with the simplest case: the semi-infinite medium consisting of a scatter-dominated medium at bottom and vacuum on top. The proper boundary condition is assumed to be a Fresnel boundary condition which gives the amount of reflected and transmitted light at a smooth boundary dependent on the ratio of refractive indices.

3.1.1 Fresnel Reflection

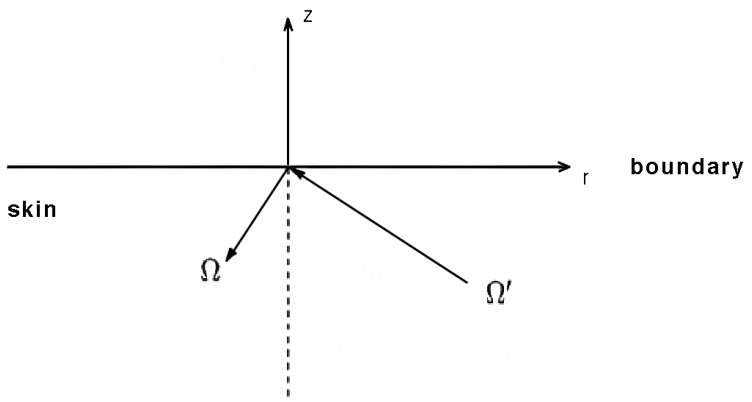

Figure 3.1: Fresnel reflection at the surface in sectional view.

Vectors Ω' and Ω give the directions of upcoming and reflected light Φ respectively. Fresnel's law of reflection states that on the boundary we have:

$$\Phi(x,\Omega,t)|_{z=0} = R(\Omega')\Phi(x,\Omega',t)|_{z=0} \quad , \quad (x,t) = (r,z,t) \in I\!R^3 \times I\!R^+ \quad , \quad \Omega,\Omega' \in S^2 \quad , \tag{3.11}$$

where $R(\Omega')$ is the reflection function given in Fresnel's law (in the case of unpolarized light)

$$R(\Omega') = \frac{1}{2}\left[\frac{n_m\cos\theta_v - n_v\cos\theta'}{n_m\cos\theta_v + n_v\cos\theta'}\right]^2 + \frac{1}{2}\left[\frac{n_m\cos\theta' - n_v\cos\theta_v}{n_m\cos\theta' + n_v\cos\theta_v}\right]^2 \quad , \tag{3.12}$$

where n_m and n_v are the refractive indices of medium and vacuum respectively, θ, θ' are the polar angles of direction Ω, Ω' resp. and θ_v depends on θ' by Snell's law:

$$\frac{\sin\theta_v}{\sin\theta'} = \frac{n_m}{n_v} \quad .$$

Remark 3.2 *For practical situations, function 3.12 can sufficiently be approximated by the piecewise constant function*

$$R^*(\Omega') = \begin{cases} 1 & \theta_c \leq \theta' \leq \frac{\pi}{2} \\ R_0 & 0 \leq \theta' \leq \theta_c \end{cases} \quad , \tag{3.13}$$

with the critical angle of total reflection $\theta_c = \arcsin \frac{n_v}{n_m}$.

Applying an idea of Marshak [43], we are able to get the Fresnel condition making the ansatz:

$$\int\limits_{S^2/2} \Phi(x,\Omega,t) Y_{k,l}(\Omega) d\Omega = \int\limits_{S^2/2} R(\Omega') \Phi(x,\Omega',t) Y_{k,l}(\Omega') d\Omega' \quad . \tag{3.14}$$

We expand the product $\Phi \cdot Y_{k,l}$ with the spherical harmonics $Y_{k,l}$ to the first order and get the approximation:

$$\Phi^*(x,\Omega,t) \simeq \frac{1}{4\pi}\Phi(x,t) + \frac{3}{4\pi} J(x,t) \cdot \Omega \quad .$$

Thus we can write both sides of 3.26 as

$$\int\limits_{S^2/2} \Phi^*(x,\Omega,t) d\Omega \simeq \frac{\Phi(x,t)}{4} + \frac{J(x,t)}{2} \quad ,$$

and

$$\int\limits_{S^2/2} R(\Omega') \Phi^*(x,\Omega',t) d\Omega' \simeq R_\phi \frac{\Phi(x,t)}{4} - R_j \frac{J(x,t)}{2} \quad ,$$

where

$$R_\phi = \int\limits_0^{\pi/2} 2 \sin\theta \cos\theta R(\theta) d\theta \quad ,$$

$$R_j = \int\limits_0^{\pi/2} 3 \sin\theta \cos^2\theta R(\theta) d\theta \quad .$$

Finally, ansatz 3.26 reduces to

$$\frac{\Phi(x,t)}{4} + \frac{J(x,t)}{2} = R_\phi \frac{\Phi(x,t)}{4} - R_j \frac{J(x,t)}{2} \quad , \tag{3.15}$$

$$\text{or} \qquad \Phi(x,t) = \frac{1+R_j}{1-R_\phi}(-2J(x,t)) \quad .$$

3.1.2 The Extrapolated Boundary

The boundary condition we just derived, represents the fresnel law at a boundary in the diffusion approximation. It has the form of a mixed boundary condition. Using the method of images, we can easily transform this condition to a *Dirichlet* boundary condition above the physical boundary at a so called *extrapolated boundary* [17]. We assume that on the physical boundary we have $\Phi(x,t)|_{z=0} > 0$. If we further assume the light source Q to be positioned inside the medium (see also the next subsection) we can infer that $\Phi'(x,t)|_{z=0} = \frac{\partial}{\partial z}\Phi(x,t)|_{z=0} < 0$. We are thus able to extrapolate $\Phi(x)$ above the physical boundary by a distance Δ such that we have:

$$\Phi(x,t)|_{z=\Delta} = 0 \qquad , \qquad \Delta = \frac{\Phi(x,t)|_{z=0}}{\Phi'(x,t)|_{z=0}} \quad . \tag{3.16}$$

Substituting 3.15 into 3.16 and using Fick's law we get:

$$\Delta = 2\frac{1+R_j}{1-R_\phi} \cdot D = \frac{1+R_j}{1-R_\phi} \cdot \frac{2}{3} l_{\text{tr}} \quad , \tag{3.17}$$

where $l_{\text{tr}} = 1\text{mfp}$, Δ is called the *extrapolation length.*

3.1.3 Source Considerations

Following remark 3.1, a directed point source situated at the top of skin in tissue optics is usually substituted by an isotropic point source located at $z_0 = 1\text{mfp}$ inside skin, called a *virtual scattering light source*:

$$Q(r,z,\theta,t)|_{r=z=0} = Q(t)\delta(x)\delta(\theta-\theta_0) \quad \longmapsto \quad Q(r,z,t)|_{r=0,z=-z_0} = Q(t)\delta(x-z_0) \quad . \tag{3.18}$$

The advantage of replacing the directed source is that in the latter case we have a fundamental solution for equation 3.5 if we set the diffusion coefficient constant. It is simply written as:

$$\Phi(|x|,t) = \frac{c}{(4\pi Dct)^{3/2}} \cdot \exp(-\frac{|x|^2}{4Dct} - \mu_a ct) \quad , \quad (x,t) \in I\!R^3 \times I\!R^+ \quad . \tag{3.19}$$

To get the DC mode, the time derivative in equation 3.5 is set to zero, the resulting fundamental solution in this case reads:

$$\Phi(|x|) = \frac{1}{4\pi D|x|} \cdot \exp(-\sqrt{\frac{\mu_a}{D}} \cdot |x|) \quad , \quad x \in I\!R^3 \quad . \tag{3.20}$$

To fulfill the extrapolated boundary condition, we have to simply add a negative virtual scattering light source at a distance $2 \cdot (\Delta + z_0)$ above the physical boundary. In DC mode we get the model function:

$$\Phi_{\text{tot}}(x) = \Phi(x - z_0) - \Phi(x + z_B) \quad , \tag{3.21}$$

with

$$z_B = 2 \cdot (\Delta + z_0) \quad , z_0 = \mu_t \quad ,$$

where Φ is the fundamental solution 3.20 .
Haskell et al. proposed a modification of model function 3.21 which takes into account that on the physical boundary the detected signal has contributions from the fluence Φ and the flux $J = \frac{\partial \Phi}{\partial z}$, [21]. The total signal is then given by:

$$\Phi_{\text{Haskell}}(x)|_{z=0} = \frac{1 - R_\phi}{4} \cdot \Phi_{\text{tot}}(x)|_{z=0} + \frac{1 - R_j}{2} \cdot \frac{\partial}{\partial z} \Phi_{\text{tot}}(x)|_{z=0} \quad , \tag{3.22}$$

where the precise linear combination of fluence and flux is a function of the numerical aperture of the fiber. For applications of this method we refer to [17] [21] [33] [46].

3.1.4 Estimates

In order to justify the diffusion approximation of the RTE, we give a pointwise, i.e. L^∞ estimate. Therefore, we consider the stationary counterpart of the Cauchy problem as given in chapter 2. The following theorem compares a solution of the stationary transport problem in the case of a scaled medium with a solution of the appropriate stationary diffusion problem. Again, we refer to [15] for further details and proofs.

Theorem 3.1 *We assume the following regularity conditions:*

$$\mu_s(x) \in C^{2,\alpha}(V) \ , \quad \textit{and} \quad q(x), \mu_a(x) \in C^{1,\alpha} \ , \quad V \subset I\!R^3 \textit{ open, bounded}^1,$$

then the unique solution u_ϵ in $L^\infty(V \times S^2)$ of the stationary transport problem:

$$\frac{1}{\epsilon}\theta \cdot \nabla u_\epsilon(x,\theta) + \left(\mu_a(x) + \frac{1}{\epsilon^2}\mu_s(x)\right) u_\epsilon(x,\theta) = \frac{1}{\epsilon^2}\mu_s(x) \int_{S^2} \eta(\theta \cdot \theta') u_\epsilon(x,\theta') d\theta' + q(x,\theta) \quad ,$$

$$\textit{for} \quad (x,\theta) \in V \times S^2 \quad \textit{and} \quad u_\epsilon|_{\Gamma_-} = 0 \quad ,^1$$

[1] In the case where V is unbounded, we need a further condition at infinity: $\lim_{|x| \to \infty} q = 0$.

and the unique solution u in $L^\infty(V)$ of the stationary diffusion problem:

$$-\frac{\partial}{\partial x_i}\left(D(x)\frac{\partial u(x)}{\partial x_j}\right)+\mu_a(x)u(x)=q(x) \quad ,$$
$$for \quad x\in V \quad and \quad u|_{\partial V}=0 \quad ,$$

satisfy:

$$\|u_\epsilon-u\|_{L^\infty(V\times S^2)}\leq \epsilon\, C_q \quad ,$$

with a positive constant C_q depending on q.

We emphasize the fact that the previous theorem assumes the Dirichlet boundary condition to be fulfilled at direct neighbourhood of the scattering medium. A virtual scattering light source, as constructed previously would therefore approach the extrapolated boundary in the case $\epsilon \to 0$, if we would transfer this theorem to the case of an extrapolated boundary condition. However, a consistent formal framework for this case would need a two-scaled medium, thus leading to $\epsilon \to \infty$ in the vacuum area between the physical boundary and the extrapolated boundary.

3.2 Two-Layer Models

We will consequently improve the halfspace model of the preceding section and introduce two-layer models in order to simulate the *dermis-subcutis* structure of skin [2]. This structure is mainly given by a distinct pair of (μ_a, μ_s') for each of the layers. Additionally, some models allow a refractive index mismatch between the layers if suited. There are roughly two methods distinguishable: *fourier space models* and *models in real space*; both will be proposed in the following.

3.2.1 A Fourier Space Model

The fourier space model of Kienle et al. is of great importance in the imaging community to model the dermis-subcutis structure in the refractive index matched case. In addition, this model serves as a basis for hybrid methods which include Monte-Carlo simulations in order to improve the accuracy of the model in the vicinity of a directed light source [1] [2] [34] [35]. Our starting point is diffusion equation 3.5 transformed to DC mode, in the inhomogeneous case for a virtual scattering light source situated in the top layer, and in the homogeneous case for the bottom layer:

$$-\nabla\cdot D\nabla\Phi(x)+\mu_a\Phi(x)=\begin{cases}\delta(x-z_0) & 0\geq z>l\\ 0 & l\geq z\end{cases} \quad , \tag{3.23}$$

[2] We recall that: $\Gamma_- := \{(x,\theta)\in\partial V\times S^2; n\cdot\theta<0\}$.

[2] "two-layer" means one layer and a halfspace beneath.

for $x \in I\!R^3$ and layer-thickness $|l|$.
Assuming translational invariance, these equations are transformed to ordinary differential equations using a two-dimensional Fourier transform:

$$\phi(s,z) = \int_{-\infty}^{\infty}\int_{-\infty}^{\infty} \Phi(x,y,z)\exp[i(s_1x + s_2y)]dxdy. \tag{3.24}$$

We apply transformation 3.24 to equation 3.23 and obtain

$$\begin{aligned} \frac{\partial^2}{\partial z^2}\phi_1(s,z) - \alpha_1^2\phi_1(s,z) &= \frac{1}{D}\delta(z-z_0), \qquad 0 \geq z > l, \\ \frac{\partial^2}{\partial z^2}\phi_2(s,z) - \alpha_2^2\phi_2(s,z) &= 0, \qquad l \geq z \quad , \end{aligned} \tag{3.25}$$

where

$$\alpha_i^2 = \frac{(D_i s^2 + \mu_{ai})}{D_i} \quad , \quad s^2 = s_1^2 + s_2^2 \quad , \quad i = 1,2 \text{ indicating the layers.}$$

The following boundary conditions are applied:

$$\begin{array}{llcll} \text{i.} & \phi(s,\Delta) & = & 0, & \text{extrapolated boundary condition ,} \\ \text{ii.} & \phi(s,-\infty) & = & 0, & \text{boundary condition at infinity,} \\ \text{iii.} & \frac{\phi_1(s,l)}{\phi_2(s,l)} & = & 1, & \text{continuity of the fluence,} \\ \text{iv.} & D_1\frac{\partial\phi_1(s,z)}{\partial z}|_{z=l} & = & D_2\frac{\partial\phi_2(s,z)}{\partial z}|_{z=l}, & \text{continuity of flux.} \end{array} \tag{3.26}$$

Conditions iii. and iv. apply at the boundary between the layers and are fulfilled in the matched refractive index case only [20]. Applying boundary conditions 3.26, the solution of equation 3.25 at the top boundary is given by (see also [30]):

$$\begin{aligned} \phi(s,z)|_{z=0} &= \frac{\sinh(\alpha_1(\Delta+z_0))}{D_1\alpha_1)}\frac{D_1\alpha_1\cosh(\alpha_1(l-z)) + D_2\alpha_2\sinh(\alpha_1(l-z))}{D_1\alpha_1\cosh(\alpha_1(l+\Delta)) + D_2\alpha_2\sinh(\alpha_1(l+\Delta))} \\ &- \frac{\sinh(\alpha_1(z_0-z))}{D_1\alpha_1} \quad . \end{aligned} \tag{3.27}$$

We now have to transform solution 3.27 back to real space. As we assume cylinder symmetry, the two-dimensional fourier transform can be written as a *Hankel transform*, which in our case is given by:

$$\Phi(r,z)|_{z=0} = \frac{1}{2\pi}\int_0^{\infty}\phi(s,z)sJ_0(sr)ds \quad , \tag{3.28}$$

where J_0 is the Bessel-function of zeroth order.
The evaluation of this integral is a crucial step in solving this two-layer model, several authors have focussed on it [41] [59]. Another relevant point of fourier-space models in general is the number of detectors which in our case amounts to 12, which yields oscillating solutions in space for the forward problem. To have smooth solutions, several hundered widespread detectors are needed as it is e.g. the case for the SCATTI imager described in [23]. For the inverse problem, this raises the computation costs of calculating the Hankel transform to several hours on a usual workstation. G. Alexandrakis (HRCC, Hamilton, Canada) proposed in his PhD thesis a hybrid approach based on this two-layer model and Monte-Carlo simulations to handle short source-detector distances [2]. In a discussion, he clearly stated that his experiences concerning calculation times confute effectivity for the in vivo setting.

3.2.2 Models in Real Space

In section 3.1, a halfspace model has been constructed adding a negative light source to the positive one. Consequently it is possible to add on further boundary conditions by adding further virtual light sources.
To do this, we define two operators R_d and R_c which map light sources Φ given by the time-dependent fundamental solution 3.19 and situated at $\tilde{x} = (0, \tilde{z})$ to their images:

$$\Phi(0,\tilde{z},t) \;\mapsto\; R_d\Phi(0,\tilde{z},t) \;:=\; -\,\Phi(0,z_B(\Delta,\tilde{z}),t) \tag{3.29}$$

$$\Phi(0,\tilde{z},t) \;\mapsto\; R_c\Phi(0,\tilde{z},t) \;:=\; (G*\Phi)(0,z'_B(\Delta',\tilde{z}),t) \quad . \tag{3.30}$$

R_d is known to fulfill a Dirichlet condition at an extrapolated boundary situated at Δ with the arising image source situated at $z_B(\Delta,\tilde{z})$, as needed to construct a semi-infinite medium.
The convolution operator R_c is needed to fulfill a second boundary condition in order to represent a second layer. In analogy to the light source created by the operator R_d, whose position is dependent on two degrees of freedom $(\Delta,\tilde{z})$, the light source created by the operator R_c is dependent on $(\Delta',\tilde{z})$. We propose two useful boundary conditions fulfilled at Δ', dependent on the actual medium setting:

i. Index mismatched case: the medium beneath the second boundary is not scattering (turbid slab geometry). Δ' in this case fixes the position of a second extrapolated boundary situated beneath the second physical boundary:

$$G = -\delta(x - z'_B) \quad .$$

ii. Index matched case: the medium beneath the second boundary is scattering. We assume continuity of flux and fluence at Δ', as proposed in 3.26. Δ' in this case serves as a parameter which is related to the scattering properties of the bottom halfspace:

$$G \hat{=} \text{ Gaussian kernel (proposed)} \quad .$$

Figure 3.2 shows a coordinate system with notations for the extrapolated boundaries as well as the positions of the light sources situated on the z-axis.

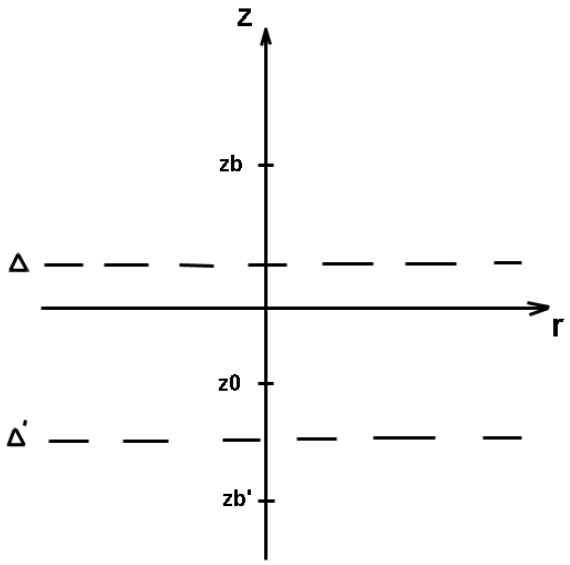

Figure 3.2: Physical boundary (r-axis) as well as extrapolated boundaries and positions of light sources.

To take into account the simultaneous presence of the Dirichlet boundary condition at the top boundary and one of the former conditions, we have to iterate the application of boundary conditions and therefore of the operators. One gets the following expression for

the light intensity at the top boundary (see also [53]):

$$\Phi_{\text{tot}}(x,t)|_{z=0} = \left\{ \left[1 + (1+R_d) \sum_{n=1}^{\infty} (R_d R_c)^n \right] (1+R_d)\Phi \right\} (x,t) \quad , \quad (x,t) \in I\!R^3 \times I\!R^+ \quad . \tag{3.31}$$

To reduce computation costs, the series is usually truncated after $n = 2$. Case **i.** corresponds to the models of Wang [55] or Contini et al. [13] to model turbid slabs. Case **ii.** is related to a model of Tualle et al. [53] extended by the proposition of the Gaussian convolution kernel. It is also possible to merge cases **i.** and **ii.** to a model that provides two index mismatches and scattering inside the bottom halfspace, which is left here.

Remark 3.3 Reasons for taking the Gaussian in case ii.
At first, it is not clear which convolution kernel should be used in case **ii.** *and whether such a computation could be done analytically, or numerically and therefore time consuming. In order to overcome this awkwardness we propose the following strategy:*
It is a classical result that the solution of a time-dependent diffusion process with no absorption is given by a Gaussian function with increasing variance in time. In the case of skin tissue where we have almost no absorption in comparison to scattering, the approximation $\mu_a = 0$ *is therefore conceivable. As the convolution in 3.30 performs further scattering inside the bottom halfspace of already scattered light coming from the top layer, translation to arithmetics of Gaussian functions therefore yields the convolution of a Gaussian by a Gaussian which is nothing but a spreading of a Gaussian. The operator* R_c *in this case just substitutes a variance by a greater variance.*

We have to annotate that our measurement setting works in DC mode. Therefore, the proposition of remark 3.3 is not of practical benefit for our studies. Nevertheless, it may be significant for noninvasive measurements in general: it is not yet fully clarified how the model of Tualle et al. motivates the use of a certain convolution kernel in the **ii.** case and how the degrees of freedom of the numerous virtual light sources are mapped to skin optical properties.

3.3 Anisotropic Diffusion - a Heuristics

In the preceding sections we dealt with some possibilities of properly applying boundary conditions within the diffusion approximation. We now want to present a heuristics to model the trait of a directed light source introducing a proper class of functions detached from the framework of fundamental solutions. This class of functions is constructed replacing the diffusion constant D in equation 3.20 by a symmetric positive definite diffusion tensor

$\tilde{D} \in \mathbb{R}^{3\times 3}$. In this way, we are able to change the trait of a light source to be a rotational ellipsoidal in space (in [56] this type is called *anisotropic diffusion* for the case of absent absorption). In our application, we have to assume that the ellipsoidal trait of the source will change fast in space to become a spheroidal trait. The assumption that isosurfaces of light intensity change in this characteristic manner is motivated by experiments where light is radiated obliquely into skin and resulting isolines of the reflected light on the boundary are egg-shaped i.e. the isolines eccentricity in direction of the light source differs from the eccentricity in the opposite direction. Moreover, this difference vanishes a few mfp apart from the source; more findings concerning probes with an oblique light source are treated in the PhD thesis of Marcus Hermann (Roche diagnostics GmbH) (to be published).
We model this behaviour by setting $\tilde{D}$ dependent on the distance from the source:

$$\tilde{D} = \tilde{D}(|x|) := \begin{pmatrix} D_1(|x|) & 0 & 0 \\ 0 & D_2(|x|) & 0 \\ 0 & 0 & D_3(|x|) \end{pmatrix} \quad , \quad D_1(|x|) = D_2(|x|) \quad . \tag{3.32}$$

In DC mode we arrive at the following expression:

$$\Phi(|x|) = \frac{1}{4\pi \left|\tilde{D}(|x|)x\right|} \cdot \exp\left(-\sqrt{\mu_a} \left| \begin{matrix} D_1^{-1/2}(|x|) \cdot x_1 \\ D_2^{-1/2}(|x|) \cdot x_2 \\ D_3^{-1/2}(|x|) \cdot x_3 \end{matrix} \right| \right) \quad , \quad x = (x_1, x_2, x_3)^T \in \mathbb{R}^3 \quad . \tag{3.33}$$

Figure 3.3 illustrates a plot of isosurfaces for Φ dependent on different ratios of $D_{1,2}/D_3$.
As we are interested in the light intensity at an array on the top of skin, expression 3.33 reduces to:

$$\Phi(|x|)|_{x_2=x_3=0} = \frac{1}{4\pi D_1(|x|)|x|} \cdot \exp\left(-\sqrt{\frac{\mu_a}{D_1(|x|)}} \cdot |x| \right) \quad , \quad x \in \mathbb{R}^3 \quad . \tag{3.34}$$

To answer the question, which is the functional behaviour of $D_1(|x|)$, we have to put up a heuristics: Since $D_1(|x|)$ is influenced by scattering events and since the radiation gets isotropic after a few of them it is proximate to take the function:

$$D_1(|x|) = D\left[1 - a \cdot b \cdot \exp(-a \cdot |x|)\right] \quad , \quad a, b \in \mathbb{R} \quad . \tag{3.35}$$

This function corresponds to the seceding probability of a photon being still unscattered as it travels through the medium (we leave out the $1/|x|^2$-factor for reasons of consistency and get the limit of isotropic diffusion for $a = 0$). The *anisotropy parameters* a and b have to be estimated using in vivo or skin phantom measurements, a respective fit result is given in appendix A.
We emphasize that a space-dependent diffusion coefficient is incompatible with the fundamental solution of equation 3.5 and its steady-state counterpart for the case $Q(x) = \delta(x)$.

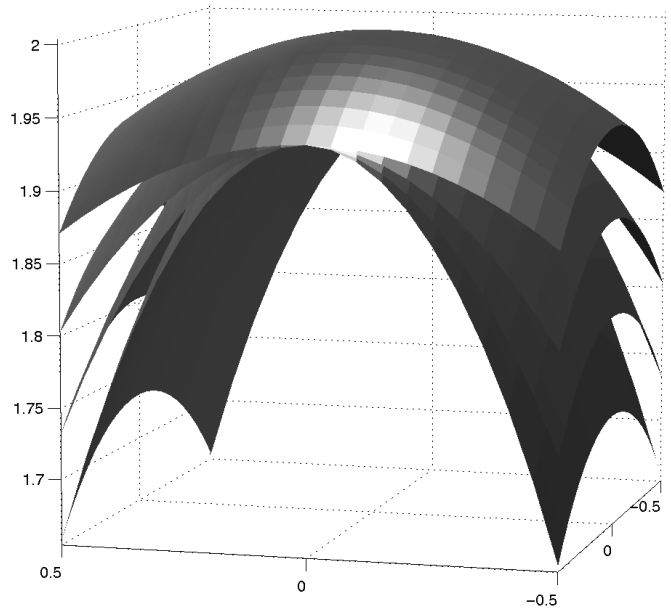

Figure 3.3: Isosurfaces of Φ for anisotropic diffusion (arbitrary units in (x_1, x_2, x_3)-space).

However the function class given by 3.33 is a solution of equation 3.5 with an extended source $Q(x)$:

$$-\nabla \cdot \tilde{D}(|x|)\nabla\Phi(|x|) + \mu_a\Phi(|x|) = Q(x) \quad , \quad x \in I\!R^3 \quad . \tag{3.36}$$

In appendix A we give the appropriate expression for $Q(x)$. In this way, we simulate light propagation issued by a sharp, directed light source in a homogeneous medium by a spatially varying medium (via the virtual diffusion tensor $\tilde{D}(|x|)$) and a virtual, extended light source $Q(x)$.

3.4 Evaluation

The diffusion approximation of the RTE has been treated in detail in order to construct layered boundary models of skin. We summarize the advantages and disadvantages of this approach:
The diffusion equation has a very simple fundamental solution whose applicability is restricted to an infinite medium at first. Building linear combinations of such fundamental solutions, it is possible to meet fresnel boundary conditions in order to construct a halfspace, or, if we take infinitely many terms, to represent a multi-layer setting. Alternatively, it is possible to transform the diffusion equation to fourier space, meet a boundary condition there and to numerically back-transform the solution to real space leading to difficulties concerning e.g. calculation times.
Each of the multi-layer models suggested treats incoherent boundary scattering only. This means that no phase relations are induced by multiple scattering between boundaries. Therefore, the layer thickness for each of the multi-layer models has to be greater than at least 1mfp. This fact has to be taken into account if one tries to model boundary scattering within the epidermis whose thickness is below 1mfp. A layered model of the epidermis is necessary because the optical properties of the epidermis are supposed to be strongly varying during a measurement period which in turn causes partly strong artefacts. The applicability of the proposed models is therefore restricted.
It is of course an interesting question why we treat the diffusion approximation of the RTE exclusively. Especially at small source-detector distances in DC mode and at small times in the time-domain the diffusion approximation is inaccurate as comparisons to Monte-Carlo simulations reveal [1] [23]. Therefore, an improvement of the light propagation model is desired. The interested reader may take a look at certain attempts to model light scattering in tissue using higher approximations of the RTE. Concerning the next higher approximation (P_3) we refer to the article [49] and the diploma thesis [57] that was motivated by Boehringer Mannheim GmbH. The latter title clearly stated the result that it is not possible to effectively solve the related inverse problem of identifying the optical parameters (μ_a, μ_s) within the P_3 approximation applying mixed Fresnel/vacuum boundary conditions in three space dimensions in less than a week on a usual workstation. This negative result has been confirmed in a discussion with the author. However to our knowledge, a rigorous development of error estimates for the P_3 approximation in the case of mixed Fresnel/vacuum boundary conditions remains open.

Chapter 4

Implementation

Sensitivity matrices are introduced in order to assess a skin model in respect of its ability to map reflectance changes to specific parameter changes.

4.1 Sensitivity Analysis

The sensitivity of a function $y(r,P) = y(x,P)|_{z=0}$ at a source-detector distance r with respect to a parameter $p_j \in P \subset I\!R^m$, P a vector of parameters, is defined by:

$$S_{p_j}(r,P) \;:=\; -\frac{\partial(y(r,P))}{\partial p_j} \quad , \quad y(r,P) \in C^1 \quad . \tag{4.1}$$

We discretize the distance r to the vector $r = (r_1, r_2, ...) \in I\!R^n$ and get a sensitivity matrix $S \in I\!R^n \times I\!R^m$

$$S \;:=\; \begin{pmatrix} S_{p_1}(r_1,P) & \cdots & S_{p_m}(r_1,P) \\ \cdot & & \cdot \\ \cdot & & \cdot \\ S_{p_1}(r_n,P) & \cdots & S_{p_m}(r_n,P) \end{pmatrix} \quad . \tag{4.2}$$

In the following we distinguish between the sensitivity S_p^I of a measured signal with respect to a parameter p and the sensitivity S_p^Φ of a proposed model with respect to a model parameter.

4.1.1 Ill-Posedness, Optimal Probes and Killing Factors

We follow the treatment of Hadamard to define *well-posedness* [42]:

Definition 4.1 *Regard a mapping $A : X \mapsto Y$ between topological spaces X and Y respectively. The problem (A, X, Y) is called well-posed if*

i. $Af = g \quad , \quad \forall g \in Y$ *has a solution*

ii. *this solution is unique*

iii. *the solution depends continuously on the data*

if one of these conditions fails the problem is called ill-posed.

Therefore, a homeomorphism between topological spaces defines a well-posed forward and inverse problem which is expressed by the demands on continuity and uniqueness in the previous definition. An ill-posed problem therefore weakens the topology of a parameter space to the topology of a signal space: the information content of the parameter space is not represented by the measured signal.
The only way to get back a homeomorphism is to weaken the toplogy of the parameter space, which is also called a *regularization* of the problem. Important examples of regularizations are given e.g. for the Radon transform which is an ill-posed problem at first but yields very useful results after applying regularization filters to the data [42].
As already stated, diffusion processes which arise in scatter dominated media are characterized by a strong weakening effect on the topology of their solution[1], furthermore all solutions are in C^∞.

Excursus: Singular Values

Due to the regularizing effect of diffusion processes, the differentiability in 4.1 can be assumed concerning model equations based on the diffusion approximation. Resulting sensitivity matrices S^Φ and their singular value decompositions are thus defined.
In the case where we have as many detectors as parameters in a model equation, the value of the determinant of S^Φ gives a measure of how good signal changes ∂I are assignable to single parameter changes $\partial I|_{\partial p_j}$. Orthogonal column vectors in S^Φ therefore represent the optimal case: the value of the determinant is maximized.
In the case where we have more detectors than parameters, the determinant is replaced by the product of singular values of S^Φ. Based on a specific model an *optimal probe design* therefore maximizes the product of singular values of S^Φ with regard to optimal source detector distances, a valid model provides such an optimization to be done successfully.
Furthermore, an artefact p^* which is correctly modeled by $\tilde{\Phi}$ having a sensitivity function $S^{\tilde{\Phi}}_{p^*}(r)$ that is linear dependent to $S^{\tilde{\Phi}}_{\mu'_s}(r)$ in $S^{\tilde{\Phi}}$ is denotable a *killing factor* leading to the consequence that this artefact is not separable from scattering by the given probe design having the distance vector $r = (r_1, r_2, ...)$. In this case, a new probe design would have to be established. Separability of parameters is therefore strongly related to the notion of well-posedness: the topology of the parameter space has to be strong enough to isolate scattering from artefacts. It is dependent on the distance vector r which constitutes the probe design.

Non-Uniqueness in Diffusion-Based Tomography

If we apply fundamental solution 3.20 to 4.2 it is obvious that both $S^\Phi_{\mu_a}(r, \mu_a, \mu'_s)$ and $S^\Phi_{\mu'_s}(r, \mu_a, \mu'_s)$ are given by linear functions. Therefore $S^\Phi_{\mu_a}(r, \mu_a, \mu'_s)$ and $S^\Phi_{\mu'_s}(r, \mu_a, \mu'_s)$ are linear dependent columns of the matrix 4.2; a transport model assuming conditions 3.10 is

[1] In [42] those problems are assigned their own class: They are called *exponentially ill-posed*

thus not a valid model to separate μ_a and μ_s' [2]. In the following section, we will develop a heuristics to overcome this negative result in the vicinity of a directed light source.

4.2 A Simple In Vivo Data Evaluation Heuristics

The task of parameter separation is placed as a nonlinear parameter estimation problem:

Problem 4.1 *For given parameters* $P = (\mu_a, \mu_s', ...)^T \in \mathbb{R}^m$, *a model function* $\Phi(r_k, P)$, $r \in \mathbb{R}^n$ *and measured signals* $I(r)$, *a tupel* P^* *of parameters has to be found such that*

$$\|I(r) - \Phi(r, P)\|^2 = \sum_{k=1}^{n} [y(r_k) - \Phi(r_k, P)]^2 \quad , \quad \Phi(r, P) = \Phi(x, P)|_{z=0}$$

is minimized.

If we assume that every $\Phi(r_k, P)$ is continuously differentiable, problem 4.1 can be expressed as a sequence of linear minimization problems [51]. Therefore, we consider the functional matrix $D\Phi(r_k, P) \in \mathbb{R}^n \times \mathbb{R}^m$. Then we have:

$$\Phi(r, P^*) = \Phi(r, P) + D\Phi(r, P) \cdot (P^* - P) + h \quad , \qquad \|h\| = o(\|P^* - P\|)$$

and the following optimization problem [51]:

Problem 4.2

$$\min_{P^*} \|I(r) - \Phi(r, P) - D\Phi(r, P) \cdot (P^* - P)\|^2$$

A solution of problem 4.2 therefore fits a model based reflectance vector optimally to a measured reflectance vector.
If we consider a time series of measurements instead of spot measurements, we can take advantage of this fact, if we regard the parameter dependent counterpart $I(r_k, P(t), t)$ of $I(r_k, t)$. The mapping $I(r_k, P(t), t) \mapsto I(r_k, P(t+1), t+1)$ is then expressible by:

$$I(r_k, P(t+1), t+1) = I(r_k, P(t), t) + D\Phi(r_k, P(t), t) \cdot (P(t+1) - P(t)) \quad .$$

A temporal reflectance change (relative change) is therefore assigned the following linear form:

$$\triangle_t I(r_k, P(t), t) \ := \ \sum_{j=1}^{m} S_{p_j}^{\Phi}(r_k, P(t), t) \cdot \triangle_t P(t) \quad , \tag{4.3}$$

and the related inverse problem:

[2] Similar results are given by [5] and [44] in a more technical manner.

Problem 4.3

$$\triangle_t P(t) \;:=\; (S^{\Phi})^{-1} \cdot \triangle_t I(r_k, P(t), t) \quad . \tag{4.4}$$

The solution to this inverse problem is now simply a matrix inversion or singular value decomposition (SVD), whether S^{Φ} is square and full rank or not. Hereby any model information enters the problem via the time and parameter dependent sensitivity matrix $S^{\Phi}(P(t), t)$.

4.2.1 Applications

If we assume that in the vicinity of a directed light source the law of Lambert-Beer holds (i.e. that upper skin behaves like a cuvette) then we have $S^I_{\mu_a}(r) = \text{const} \cdot r$. If we further assume that $S^I_{\mu'_s}$ is not correctly represented by model equation 3.20 and thus $S^I_{\mu'_s}(r) \neq \text{const} \cdot r$, then problem 4.3 is easily modified to simultaneously eliminate absorption changes and changes of source light intensity (common mode changes) with $S^I_{CM}(r) = \text{const}$.
Taking the second spatial difference of $\Delta_t I(r_k, P(t), t)$ in equation 4.3 und summing up over all time intervals, we get an algorithm producing the signal Al:

Algorithm 4.1

$$Al\,(r'_k, P, T) := \sum_{t=0}^{T} \triangle_r^2 \triangle_t I(r_k, P(t), t) \tag{4.5}$$

which is insensitive with respect to μ_a and common mode changes. In the following, we consider the vector of signals $Al(r'_1, ..., r'_p)\,, \quad p = n - 2$. The near distance vector $r = (0.8, 1.2, 1.6, 2.0, 2.4, 2.8)$ [mm] of probe NIT 1.37 is therefore mapped to the vector $r' = (1.2, 1.6, 2.0, 2.4)$ [mm], with $\Delta^2 I(r) := I(r-1) - 2I(r) + I(r+1)$. We regard the values of Al to be arbitrary units for simplicity. If suited, the values are transformable to physical units applying an appropriate model to calculate values for e.g. $\triangle_r^2 S^{\Phi}_{\mu'_s}(r', P)$. In appendix B the function $\triangle_r^2 S^{\Phi}_{\mu'_s}(r', P)$ is plotted assuming the semi-infinite diffusion model given in 3.22.
Applications of algorithm 4.1 to continuous in vivo measurements show very encouraging results with respect to the absorption separating properties. Even if we know that the law of Lambert-Beer is not exactly fulfilled in skin tissue (e.g. due to the boundary structure) it seems that the power expansion of the function $S^I_{\mu_a}(r, P) = \sum_{k=0}^{\infty} a_k(P) r^k$ is clearly dominated by the second coefficient. Also interesting is the fact that the sensitivity of signal Al with respect to glucose changes is nearly exponentially decreasing for increasing source-detector distances r'. This finding agrees with calculations using model 3.22 (see also appendix B) and underpins model equation 3.20 to gain applicability apart from a directed light source (and despite the influence of boundaries).

4.2.2 Drift

Apparently converse to common mode and absorption whose sensitivity function expansions are dominated by the first and second coefficient respectively, are artefacts concerning boundary changes. Evaluations using algorithm 4.1 in some experiments show amplifications of e.g. drift artefacts. The drift artefacts are supposed to result from epidermal imbuance caused by the probe cover (which in turn would change refractive indices inside and above the epidermis). This finding emphasizes the fact that algorithm 4.1 treats absorption and common mode artefacts only and neglects e.g. boundary changes that also have a crucial effect on noninvasive measured signals. Using Al signals, the need to treat drift artefacts is therefore fortified. We have to face this fact in the following.

4.2.3 Some Examples

First, we present some examples of a unique 5-hour in vivo experiment where glucose has been varied by an oral glucose drink after the (nearly diabetic) volunteer has been demure for several hours (so called OGT experiment). The glucose impact amounts to an amplitude of 130mg/dl and it was the goal of this run to show the impact of small glucose amplitudes on the scattering coefficient [22] .
Successively, the plots show the same experiment, first applying the fit algorithm N4 based on the semi-infinite halfspace diffusion model 3.22 implemented by M. Hermann [23] and S. Nickell [45] for Boehringer Mannheim GmbH (Fig.4.1). We see the reduced scattering coefficient μ_s' at 805nm and the interpolated reference glucose (taken by invasive spot measurements):

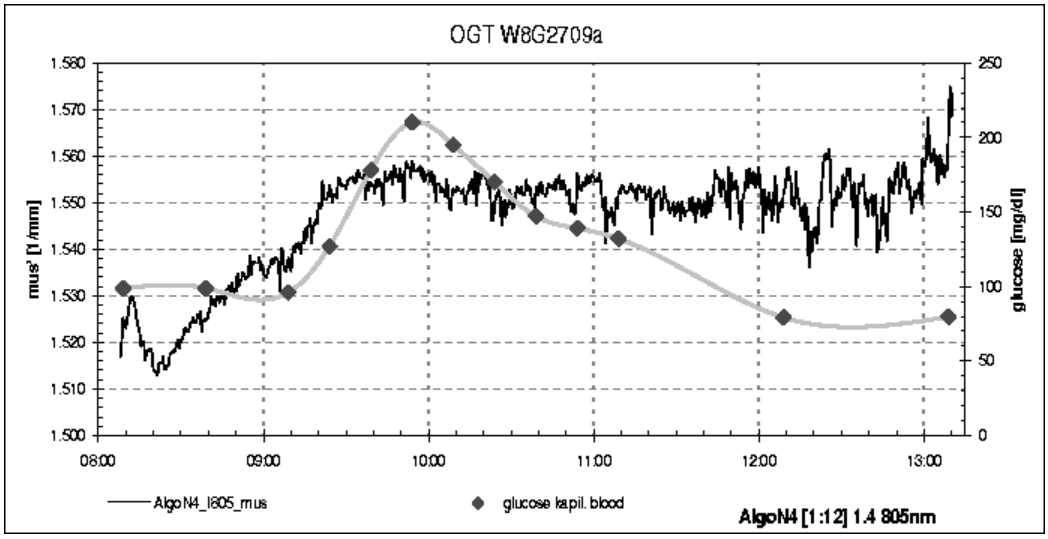

Figure 4.1: Fit result using a semi-infinte halfspace model.

Figures 4.2 to 4.5 plot the same experiment, but evaluated with algorithm 4.1 (calibrated to absolute glucose values). The $Al(r')$ signals show a more balanced behaviour which is typical for this algorithm. In order to reduce a drift artefact which is present during the whole measurement period, plots 4.3 to 4.5 have been subtracted by an exponential function whose parameters have been estimated using four reference glucose values. The use of an exponential function as drift model has been motivated by in-house (Roche) refractometer experiments where the refractometer has covered the epidermis for several hours. The half-life period of the refractometer experiments are comparable to the ones of most of the drifting OGT experiments (which amount to about 50% of the total) and lie in the range of 3 to 5 hours. Plots 4.3 to 4.5 are given the same half-life period that was estimated utilizing signal $Al(r'_1)$. They confirm the finding that the sensitivity for glucose changes decreases monotonically for increasing distances $r' = (1.2, 1.6, 2.0, 2.4)$ [mm].

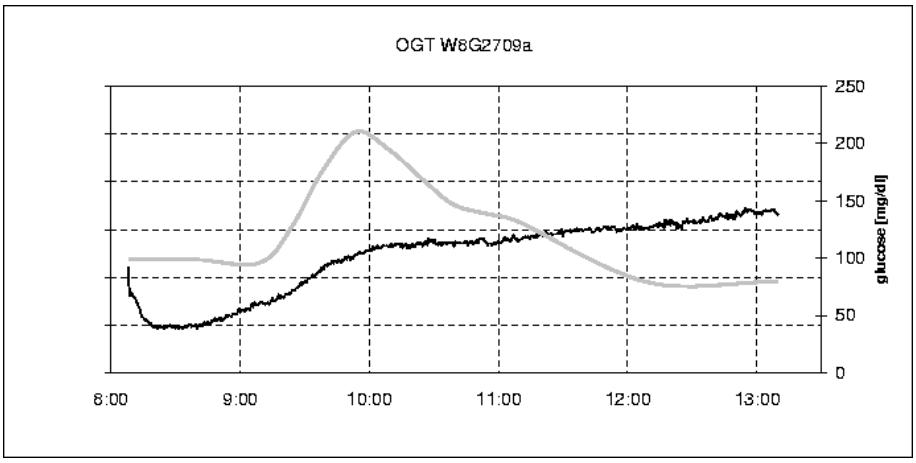

Figure 4.2: The signal $Al(r'_1)$ applied to the same data.

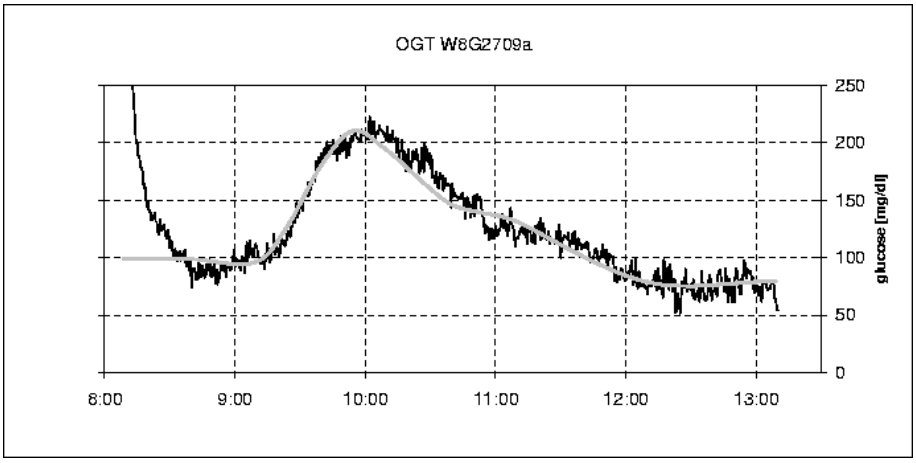

Figure 4.3: Al signal (drift removed) in direct vicinity of the source: $Al(r'_1)$.

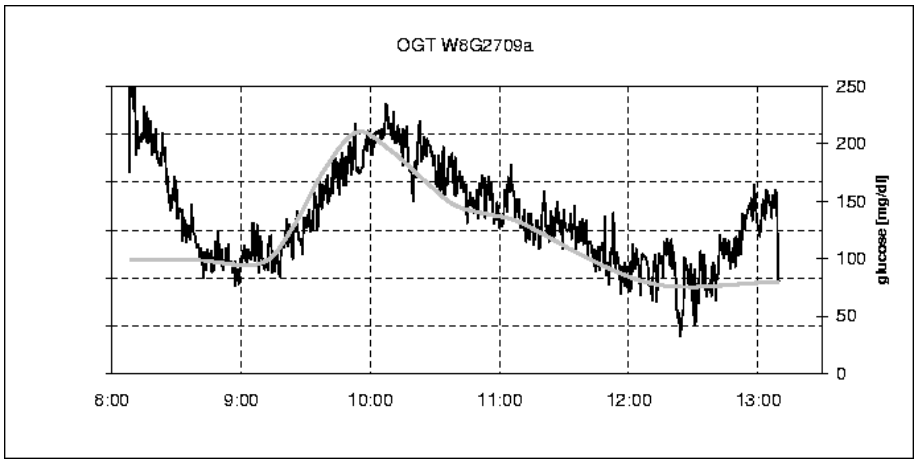

Figure 4.4: Al signal (drift removed) more distant from the source: $Al(r_2')$.

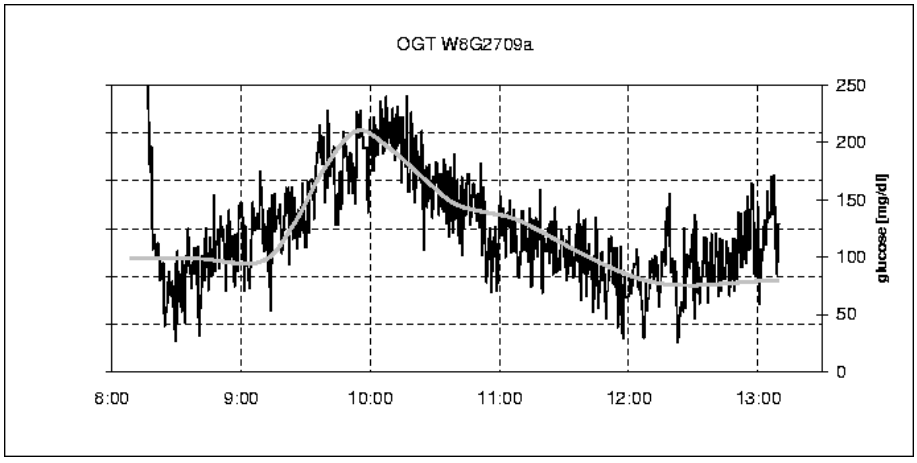

Figure 4.5: Al signal (drift removed) even more distant from the source: $Al(r_3')$.

In opposition to the preceding OGT experiment where the probe temperature has been held constant, the following experiment shows the impact of a temperature change which has been triggered outside skin by heating and cooling the probe. In figure 4.6 we see crude signals (relative signal changes $\Delta_t I(r_k, t)$) at the first four distances $r = (0.8, 1.2, 1.6, 2.0)$ [mm] of the NIT 1.37 probe using arbitrary units, and bold on top the absolute temperature T at the probes temperature sensor. The plot clearly shows that the sensitivity $S^I_{\text{Temp.}}(r) = \frac{\Delta_t I(Temp.,t)|_{\Delta\text{Temp.}}}{\Delta Temp.}$ of the measured signal with respect to temperature changes doesn't have to be constant: the signal response at $r = (1.2, 1.6, 2.0)$ [mm] changes sign in the second temperature swing.

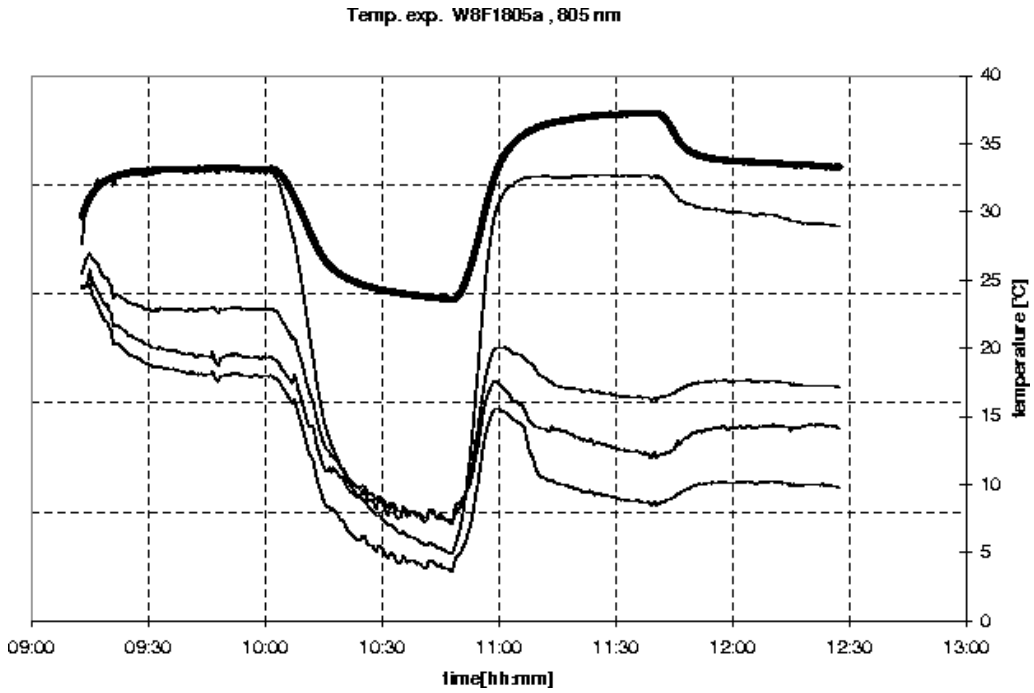

Figure 4.6: Difference in signal response at consecutive temperature variations (0.8mm thin line on top to 2.0mm on bottom).

4.3 Evaluation

The implementation of sensitivity based methods, especially findings concerning algorithm 4.1 give rise to the following statements:

1. It is possible to improve crude signal changes by the very simple evaluation algorithm 4.1 in a way that short time artefacts which are supposed to be dominated by absorption changes can be reduced significantly. Comparisons to classical fit algorithms like N4/N5 ([23] [45]) show more balanced results. Furthermore algorithm 4.1 gives a vector of time-dependent signals instead of a single $\mu_s'(t)$-signal and thus can serve as a basis for further e.g. data driven evaluation procedures in order to reduce drift artefacts.

2. The results of algorithm 4.1 partly show strong drift artefacts. A comparison to the associated crude signal changes give rise to the presumption that sensitivities of the underlying boundary effects are dominated by coefficients of higher order (concerning their power expansion) and that drifts are therefore amplified by taking the second spatial difference. Due to the great variety of possible physiological impacts of imbuance inside and above the epidermis, it is not realistic to have a simple functional description of sensitivity functions with respect to boundary changes. For the sake of an effective problem-handling, we therefore have to excurse to data driven approaches in the next chapter.

3. Concerning temperature artefacts the situation is more complicated: the sensitivities of glucose induced scattering changes and drift artefacts have to be assumed to be nearly constant during usual measurement periods (several hours) which is confirmed by the fact that calibration coefficients remain unchanged during these periods. In opposition to this, we have to assume that in some cases it is impossible to eliminate temperature artefacts by a linear transformation of detector signals with a constant coefficient in time. Therefore, we have to assume that $S_{\text{Temp.}}(r) = S_{\text{Temp.}}(r,t)$ and thus, an elimination of temperature artefacts by simply adding a multiple of the temperature sensor signal ΔT to the signal won't work.
An overview of several other artefacts occuring in noninvasive measurements such as changes of the water content of skin, body movements, oxygenation changes etc. and their impact on noninvasive signals has been given in the PhD thesis of H.-M. Klötzer (Roche diagnostics GmbH) [36].

4. It is hardly possible to give any statistical warranty for those of the above statements that need to be confirmed by appropriate investigations. This is mostly due to the fact that physiological side conditions differ significantly between the experimental runs, making the volunteers and therefore the experiments hardly comparable. Moreover, the total number of in vivo experiments under consideration amounts to about 100. This number may lie in the range of the number of more or less differing parameters triggered by anatomy or physiology. We therefore won't try to apply an according statistical framework.

Chapter 5

Excursus: Data-Driven Approaches

In this chapter, we will excurse to data-driven approaches in order to evolve our data evaluation possibilities. Recently, a new method for 'blind' data evaluation has been proposed, namely *independent component analysis* [12] which will be treated in detail. To motivate the technique, we will give a summarizing overview of the papers of A. Hyvärinen [25] and T.-W. Lee et al. [39]. First, we put up the so-called *linear mixing problem* of the hidden parameter changes $\Delta_t P(t) \in \mathbb{R}^m$ that have to be reconstructed from the observed signals $\Delta_t I(t) \in \mathbb{R}^n$ (see also equation 4.3), i.e.

$$\Delta_t I_{r_i t_k} := \frac{I_{r_i t_k} - I_{r_i t_{k-1}}}{I_{r_i t_k}} = \sum_{j=1}^{m} S_{r_i p_j} \cdot \Delta_t p_j(t_k) \quad , \quad \Delta_t I_{r_i t_k} \in \mathbb{R}^n \times \mathbb{R}^\tau$$

at τ discrete time points t_k, or in short form:

$$\forall t \; : \qquad \Delta I = S \cdot \Delta P \quad , \quad S \in \mathbb{R}^n \times \mathbb{R}^m \quad , \tag{5.1}$$

where the mixing matrix S is assumed to be constant over time.

5.1 Second-Order Methods

Contrary to the inverse problem 4.3, we now want to estimate matrix S without having a skin model to provide for S^Φ. One popular approach to find a linear transform S in 5.1 is second-order methods with important derivatives like *principal component analysis (PCA)*, sometimes called the (discrete) Karhunen-Loève transform or *factor analysis*. Both methods put an orthogonal basis inside the observed data space, thus minimizing an error functional based on mean squares. A SVD decomposition of $\Delta_t I(r,t) = U \Sigma V^T$ accomplishes this task easily, leading to a PCA subspace U and the appropriate factor loadings contained in V^T. If we drop principle components belonging to small singular values contained in Σ, we speak of a *biased* method, otherwise it is called *unbiased*.

5.2 Higher-Order Methods

We want to strengthen the requirement of uncorrelatedness of data arising from second-order methods to the notion of *statistical independence*.

Statistical independence

Denote by $u_1, u_2, ..., u_m$ some random variables with joint density $f(u_1, ..., u_m)$. The variables u_i are (mutually) independent if the density function can be factorized:

$$f(u_1, ..., u_m) = f_1(u_1)f_2(u_2)...f_m(u_m) \quad , \tag{5.2}$$

where $f_i(u_i)$ denotes the marginal density of u_i. An equivalent formulation of independence states that:

$$E\{g_1(u_i)g_2(u_j)\} - E\{g_1(u_i)\}E\{g_2(u_j)\} = 0, \text{ for } i \neq j \quad , \tag{5.3}$$

for any measurable functions g_1 and g_2. This property is sometimes called statistical independence, as compared to uncorrelatedness which is defined by:

$$E\{u_iu_j\} - E\{u_i\}E\{u_j\} = 0, \text{ for } i \neq j \quad . \tag{5.4}$$

It follows that independence is a sufficient but not a necessary condition for uncorrelatedness. But both qualtities coincide in the case when $u_1, ..., u_m$ have a joint Gaussian distribution. Due to this property, the concept of statistical independence is not advantageous for Gaussian variables.

5.2.1 Independent Component Analysis

We state two definitions of independent component analysis (ICA) that are somehow inverse to each other. In the following, the observed n-dimensional signal vector is denoted by $\Delta I = (\Delta I_1, ..., \Delta I_n)^T$. First we give a definition that states the principle of ICA:

Definition 5.1 *ICA of a signal vector $\Delta I \in \mathbb{R}^n$ consists of finding a linear transform $\Delta P = W \cdot \Delta I$, $W \in \mathbb{R}^n \times \mathbb{R}^m$ so that the parameters $\Delta P_i \in \mathbb{R}^m$ are as independent as possible, in the sense of maximizing some function $F(\Delta P_1, ..., \Delta P_m)$ that measures independence.*

This definition just says that if a measure of independence exists, ICA provides for the appropriate linear transform, no additional assumptions on the data are made. In this regard, a section below we will have to deal with contrast functions providing for manageable measures of independence for the ΔP_i. The following definition reproduces our mixing problem 5.1:

Definition 5.2 *(Jutten and Hérault [29]) ICA of a signal vector* $\Delta I \in \mathbb{R}^n$ *consists of estimating the following generative model for the sensor data:*

$$\forall t \; : \qquad \Delta I = S \cdot \Delta P \quad , \quad S \in \mathbb{R}^n \times \mathbb{R}^m \quad ,$$

again S *is assumed to be constant in time.*

It can be shown [12] that if the data does follow the generative model in definition 5.2, definitions 5.1 and 5.2 become asymptotically equivalent in a weak topology of matrix classes for certain F.

Identifiability of the ICA Model

We refer to the treatment of identifiability in [12] and [25]. For simplicity, occurance of (weak) Gaussian noise in the data will be treated like an additional independent (Gaussian) component and measured signals are assumed to be 0-1 normed. The identifyability of a class of independent components within the ICA model, where independent components inside a certain class are unique up to a permutation and scaling, can be assured if the following restrictions are imposed:

i. At most, one source is normally distributed.

ii. The number of sensors n must be at least as large as the number of parameters m, i.e. $n \geq m$.

iii. $\forall\, t$: The parameter changes $\Delta P(t)$ are mutually independent.

Referring to our mixing problem, the parameters are exactly recovered when W is the inverse of S up to a permutation and scale change:

$$P = R \cdot D = W \cdot S \quad ,$$

where R is a permutation matrix and D is a scaling matrix.

5.2.2 Applications of ICA

Contrast Functions

The notion of statistical independence between random variables yields practical results if we transfer it to equivalent concepts like *information maximation* and *negentropy maximation*. Without going into detail, we want to briefly review the basic definition of mutual information:

Definition 5.3 *The mutual information* $I(u)$ *of a measured signal vector* u *is given by the Kullback-Leibler (KL) divergence* $D(\cdot\|\cdot)$ *of the multivariate density* $f(u)$ *and the density written in product form:*

$$I(u) \; := \; \int f(u) \log \frac{f(u)}{\Pi_{i=1}^N f_i(u_i)} dx = D(\, f(u) \,\|\, \Pi_{i=1}^N f_i(u_i)\,) \quad , \quad I(u) \geq 0 \quad . \tag{5.5}$$

Thomas and Cover [14] showed that $I(u)$ is zero iff the components u_i are statistically independent. Again the concept of mutual information is easily adapted to the notion of *negentropy* which is defined as the KL divergence between the density $f(u)$ of variable u and a Gaussian distribution f_G with the same mean and covariance as $f(u)$. Finally, Girolami [19] showed that minimizing the mutual information of the components of a random vector is identical to maximizing their negentropy.
The task of finding a measure of statistical independence is now transferred to the task of finding a feasible measure of negentropy, in turn giving a measure of non-Gaussianity of a density $f(u)$ using the following definition of negentropy:

Definition 5.4 *The measure*

$$J(u) \;:=\; H_{Gauss} - H(u) \quad , \quad J(u) \geq 0 \quad , \; with \quad H(u) \;:=\; -\int f(u) \log f(u) du \quad ,$$

is called negentropy.

Due to the fact that a Gaussian variable has the largest entropy among all random variables of equal variance [14], measure 5.4 is always positive. As the exact value of $f(u)$ is usually unknown, simpler approximations of negentropy have to be considered. Jones & Simon [28] as well as Comon [12] utilized an Edgeworth expansion of 5.5 truncated at fourth-order to approximate the mutual information by:

$$J(u) \;:=\; \frac{1}{12} E\{u^3\}^2 + \frac{1}{48} \mathrm{kurt}(u)^2 \quad , \tag{5.6}$$

where the *kurtosis* is defined by:

$$\mathrm{kurt} \;:=\; E\{u^4\} - 3(E\{u^3\})^2 \quad .$$

In order to overcome non-robustness encountered with fourth-order cumulants in general and especially kurtosis [26], the framework of cumulants has been overcome. In [24] the following *contrast function* thus approximating negentropy has been proposed:

$$J_G(u) \;:=\; |E_u\{G(u)\} - E_\nu\{G(\nu)\}|^p \quad . \tag{5.7}$$

$J_G(u)$ is equipped with a smooth, non-quadratic function $G(u)$ and an exponent $p = 1, 2$ typically. For $G(u) = u^4$, J_G becomes simply the modulus of kurtosis of u, equation 5.7 therefore generalizes the moment-based approximation in 5.6. Equation 5.7 is consistent in the sense that it is always non-negative and equal to zero if u has a Gaussian distribution. The following choices of G were proposed in [25] and [26]:

$$G_1(u) = \log\cosh a_1 u \quad , \qquad G_2(u) = \exp(-a_2 u^2/2) \quad , \tag{5.8}$$

where $a_1, a_2 \geq 1$ are some suitable constants.

The FastICA algorithm

We will use the MATLAB implementation 'FastICA', provided by the *Neural Network Research Centre* at Helsinki University (www.cis.hut.fi/projects/ica/fastica) which utilizes usual numerics like e.g. a Newton iteration or Gram-Schmitt orthogonalization. For further details see e.g. [25]. We applied this algorithm to the OGT experiment of the preceding chapter at 805nm. Figure 5.1 shows the independent components that ensue after feeding the first four crude signals at $r = (0.8, 1.2, 1.6, 2.0)$ [mm] to the algorithm. We have chosen the contrast function G_2 given in 5.8. The reduction to three independent components produces one drift afflicted signal and two noisy and unspecific signals (arbitrary units) given in figure 5.1.

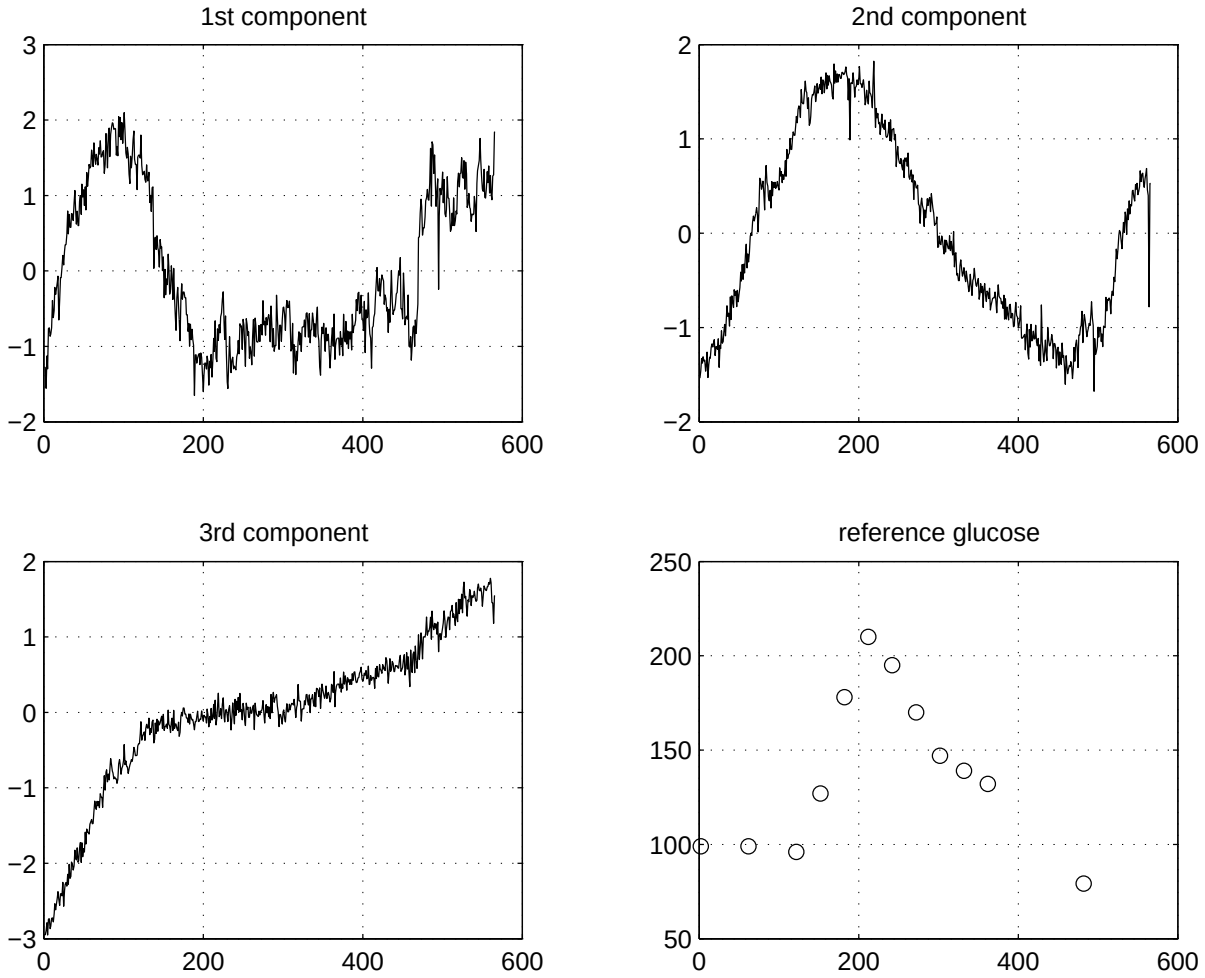

Figure 5.1: ICA applied to crude signals: The third component shows a drift afflicted signal.

ICA Meets Diffusion Theory

The results of ICA become more interesting if we take into account model knowledge which is e.g. represented by the $Al(r)$ signal, as given by the heuristics of the preceding chapter: we therefore combine model knowledge with a data driven approach. That way, ICA provides for a refinement of a given sensitivity matrix structure. We map the first four $Al(r)$ signals of the same experiment to three independent components. Figure 5.2 shows the result.

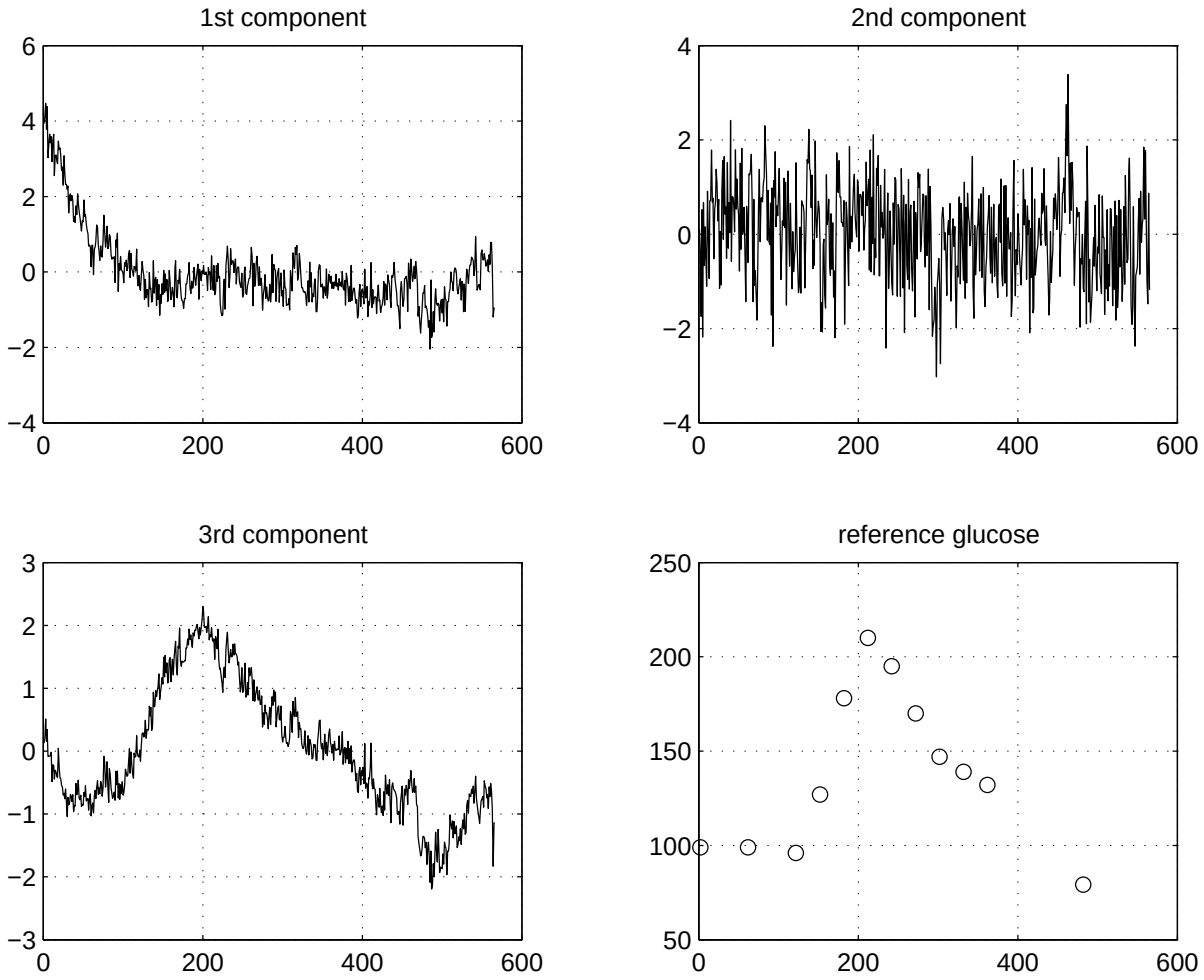

Figure 5.2: ICA applied to an Al signal.

Obviously the third component of figure 5.2 correlates to the reference glucose. Therefore, the drift pattern, which is still existent in the third component of figure 5.1 has been separated successfully.

Summary and Outlook

Summarizing our attempts to identify the light scattering coefficient of skin and its alterations in in vivo datasets, we have to make primarily the following observation: although we had to weaken our pretension to model light propagation in skin tissue within the RTE framework, the task of evaluating noninvasive measured signals entailed challenges of its own type. First, we established multi-layer skin models using the diffusion approximation of the RTE. For the skin being a scatter-dominated medium, this possibility is certainly permitted for large source-detector distances. However, skipping to short source-detector distances, a thorny problem of noninvasive diagnostics has been entered, which in this thesis has been treated by setting up a heuristics: we first stepped a little bit aside of the framework of fundamental solutions for the diffusion approximation, but related to it, constructing an virtual, extended light source thus fulfilling a diffusion equation for a proper class of functions.
For the sake of usefulness of multi-layer models in noninvasive diagnostics, we proposed a new convolution kernel to be applied to real space models like the one of Tualle et al. in time-domain.
Again, the attempt to tackle an important problem of continuous monitoring, this time occuring as drift artefacts for the in vivo setting, has been avoided within the straight diffusion theory framework: multi-layer models based on the diffusion approximation presume layer-thicknesses greater than one mfp, therefore the attempt to map drift artefacts to suitable optical effects inside or directly above the epidermis has to fail.

Finally, these findings resulted in a change of the solution strategy: the limitations of modeling within the partial differential equations framework, concerning the RTE or the diffusion approximation of the RTE, have revealed to be obvious when applied to the complexity of this special in vivo setting. In other words, it is not advisable to try to handle the complexity of this in vivo setting opposing a partial differential equation apparatus of equal complexity plus the use of a big computing device only.
After all, the connection of a simple data evaluation heuristics based on fundamental insights of light propagation in tissue with a data-driven refinement tool, namely independent component analysis, produced the best results in vivo. It will be the subject of future research to embark on this strategy. An adaptive refinement of sensitivity matrices or

qualitative statements about sensitivity matrices has to be investigated. Consequently, a measurement device which is able to attune to its wearer after a certain wearing period would result. Methods of 'hard' computing and 'soft' computing will therefore be combined in this strategy.

Acknowledgements

First of all my gratitude is expressed to Prof. Dr. Drs. h.c. W. Jäger who issued this interesting research topic to me.
I have to thank for endless trust and confidence in the last couple of years.

Sincere thanks to the whole research team at Roche diagnostics GmbH in Mannheim, dep. 'Diabetes Care - New technologies', especially to Dr. M. Hermann, Dr. H.-M. Klötzer and the project leader Dr. U. Krämer for interesting and fruitful discussions.

Last but not least my thanks are going to Dr. S. Krömker and Edward Viesel for the competent cross-reading of this thesis.

Appendix A

The anisotropic diffusion heuristics is applied to the in vivo experiment used in chapter 4, this time at 660 nm. In figure 6 we have chosen the intensity profile weighted by the square of the distance r at a single measurement point in the middle of the experiment. For the isotropic case we take the semi-infinite model as proposed in equation 3.22 ($n_{rel} = 1.4$, $\mu_a = 0.01$) and modify it to the anisotropic case replacing the diffusion constant D by the space dependent diffusion coefficient $D \cdot [1 - a \cdot b \cdot \exp(-a \cdot |x|)]$. The fit results for the resulting values D, a, b and μ_a are given in the table below.

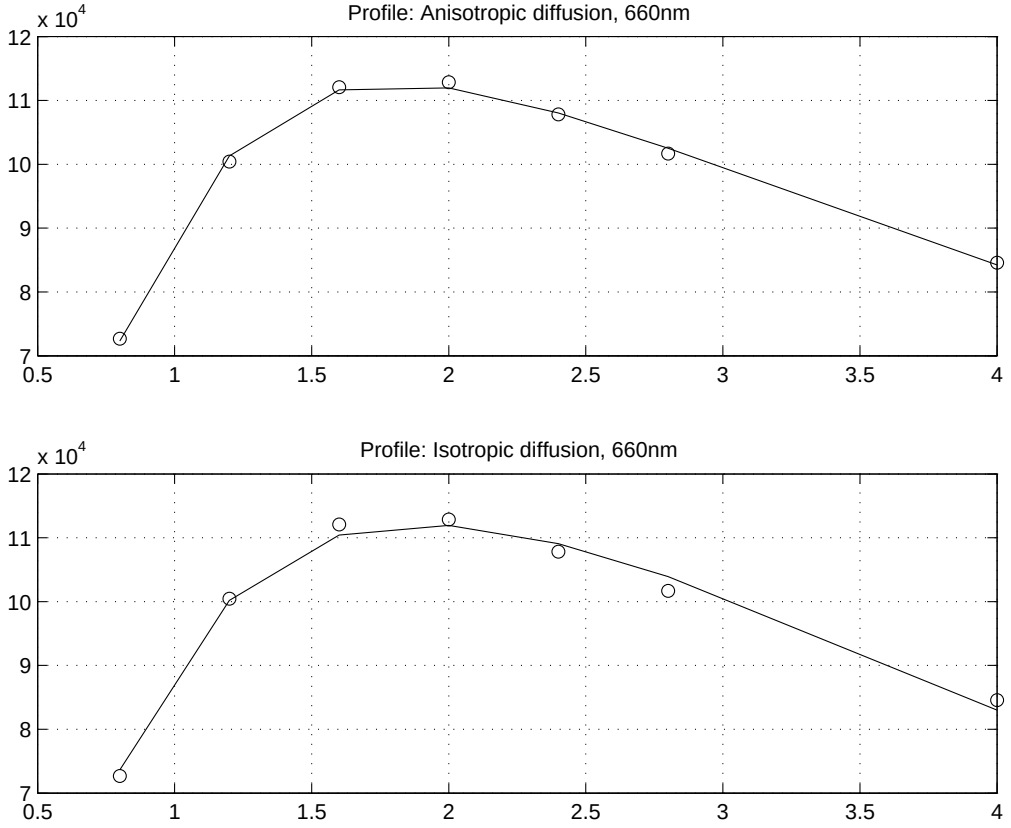

Figure 6: Plot of the measured profile $I(r) \cdot r^2$ (circles) and the model profile $\Phi(r) \cdot r^2$ for the case of isotropic and anisotropic diffusion subject to r in mm.

Fit result using first seven distances of NIT 1.37, r=(0.8,1.2,1.6,2.0,2.4,2.8,4.0)[mm]:

	$D[mm]$	$\mu_a[1/mm]$	a	b
anisotropic diffusion	0.2504	0.0124	0.4739	1.9955
isotropic diffusion	0.3213	0.0478	0	-

fit-error anisotropic diffusion	1.6411e+03
fit-error isotropic diffusion	3.7051e+03
resulting error reduction	55%

The dependency of the profile $I(r) \cdot r^2$ on the anisotropy coefficient a is plotted in figure 7.

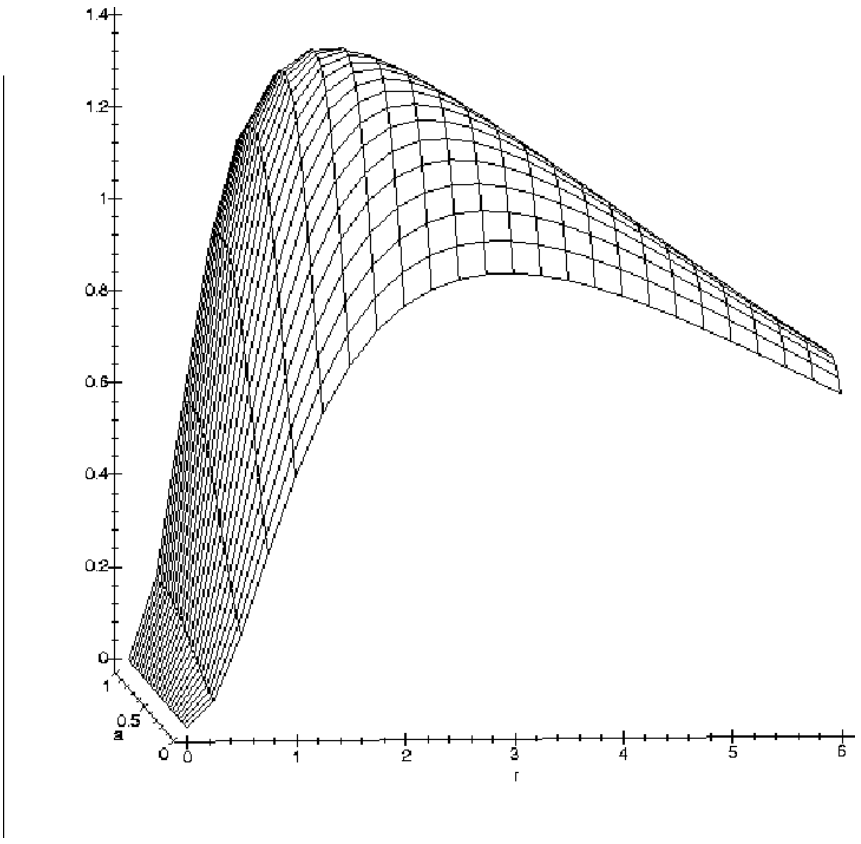

Figure 7: Profiles $\Phi(r) \cdot r^2$ for near distances dependent on a, $(b = 2, D = 0.3[mm], \mu_a = 0.01[1/mm])$.

Applying expression 3.33 to differential equation 3.36 we get the following MAPLE output:

$$Q(a_{1,3};b_{1,3};D_{1,3};\mu_a;x_1;x_2;x_3) := Q(a1,2;b1,2;D1,2;ma;x;y;z) =$$

$$-D1\,\%2\Big(\frac{3}{4}\,\frac{\%4\,D1^4\,\%2^4\,x^2}{\pi\,\%5^{5/2}}+\frac{1}{2}\,\frac{\sqrt{ma}\,D1\,\%2\,x^2\,\%4}{\pi\,\%5^{3/2}\,\sqrt{\%3}}-\frac{1}{4}\,\frac{\%4\,D1^2\,\%2^2}{\pi\,\%5^{3/2}}$$

$$+\frac{1}{4}\,\frac{\sqrt{ma}\,x^2\,\%4}{\pi\,\sqrt{\%5}\,\%3^{3/2}\,D1^2\,\%2^2}-\frac{1}{4}\,\frac{\sqrt{ma}\,\%4}{\pi\,\sqrt{\%5}\,\sqrt{\%3}\,D1\,\%2}+\frac{1}{4}\,\frac{ma\,x^2\,\%4}{\pi\,\sqrt{\%5}\,\%3\,D1^2\,\%2^2}\Big)-D1\,\%2$$

$$\Big(\frac{3}{4}\,\frac{\%4\,D1^4\,\%2^4\,y^2}{\pi\,\%5^{5/2}}+\frac{1}{2}\,\frac{\sqrt{ma}\,D1\,\%2\,y^2\,\%4}{\pi\,\%5^{3/2}\,\sqrt{\%3}}-\frac{1}{4}\,\frac{\%4\,D1^2\,\%2^2}{\pi\,\%5^{3/2}}+\frac{1}{4}\,\frac{\sqrt{ma}\,y^2\,\%4}{\pi\,\sqrt{\%5}\,\%3^{3/2}\,D1^2\,\%2^2}$$

$$-\frac{1}{4}\,\frac{\sqrt{ma}\,\%4}{\pi\,\sqrt{\%5}\,\sqrt{\%3}\,D1\,\%2}+\frac{1}{4}\,\frac{ma\,y^2\,\%4}{\pi\,\sqrt{\%5}\,\%3\,D1^2\,\%2^2}\Big)-D2\,\%1\Big(\frac{3}{4}\,\frac{\%4\,D2^4\,\%1^4\,z^2}{\pi\,\%5^{5/2}}$$

$$+\frac{1}{2}\,\frac{\sqrt{ma}\,D2\,\%1\,z^2\,\%4}{\pi\,\%5^{3/2}\,\sqrt{\%3}}-\frac{1}{4}\,\frac{\%4\,D2^2\,\%1^2}{\pi\,\%5^{3/2}}+\frac{1}{4}\,\frac{\sqrt{ma}\,z^2\,\%4}{\pi\,\sqrt{\%5}\,\%3^{3/2}\,D2^2\,\%1^2}$$

$$-\frac{1}{4}\,\frac{\sqrt{ma}\,\%4}{\pi\,\sqrt{\%5}\,\sqrt{\%3}\,D2\,\%1}+\frac{1}{4}\,\frac{ma\,z^2\,\%4}{\pi\,\sqrt{\%5}\,\%3\,D2^2\,\%1^2}\Big)+\frac{1}{4}\,\frac{ma\,\%4}{\pi\,\sqrt{\%5}}\quad ,$$

$$\%1 := 1-a2\;b2\;e^{(-a2\,\sqrt{x^2+y^2+z^2})}\quad ,$$

$$\%2 := 1-a1\;b1\;e^{(-a1\,\sqrt{x^2+y^2+z^2})}\quad ,$$

$$\%3 := \frac{x^2}{D1\,\%2}+\frac{y^2}{D1\,\%2}+\frac{z^2}{D2\,\%1}\quad ,$$

$$\%4 := e^{(-\sqrt{ma}\,\sqrt{\%3})}\quad ,$$

$$\%5 := D1^2\,\%2^2\,x^2+D1^2\,\%2^2\,y^2+D2^2\,\%1^2\,z^2\quad .$$

Q describes an anisotropic light source except for the case $a1,2=0$ (isotropic limit).

Appendix B

The decreasing sensitivity $\Delta_r^2 S^{\Phi}_{\mu_s'}(r, D)$ with respect to the distance r dependent on the diffusion constant $D := Di$ is given in figure 8, the ability of algorithm 4.1 to separate μ_a from μ_s', measured by the ratio $\Delta_r^2 \left(\frac{S^{\Phi}_{\mu_s'}(r,d)}{S^{\Phi}_{\mu_a}(r,d)} \right)$ dependent on the source-detector distance r and the separation distance between single detectors d is given in figure 9, both plots utilize the semi-infinite model as proposed in equation 3.22.

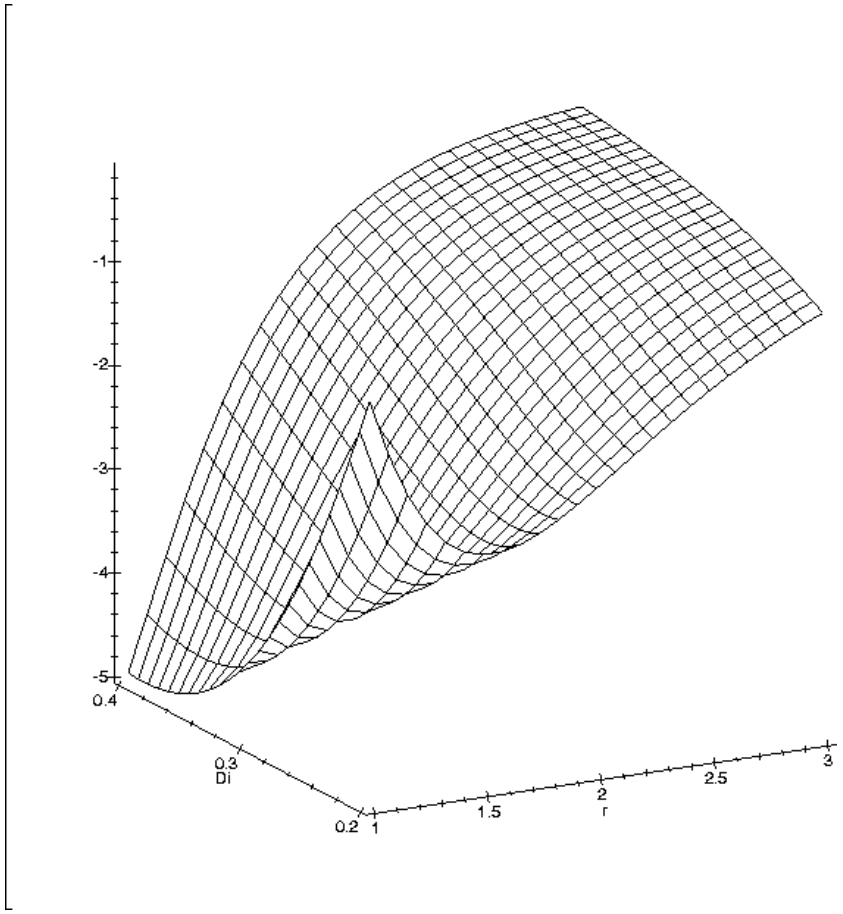

Figure 8: $\Delta_r^2 S^{\Phi}_{\mu_s'}(r, Di)$ - zero is on top of plot, ($n_{rel} = 1.4$, $\mu_a = 0.01[1/mm]$).

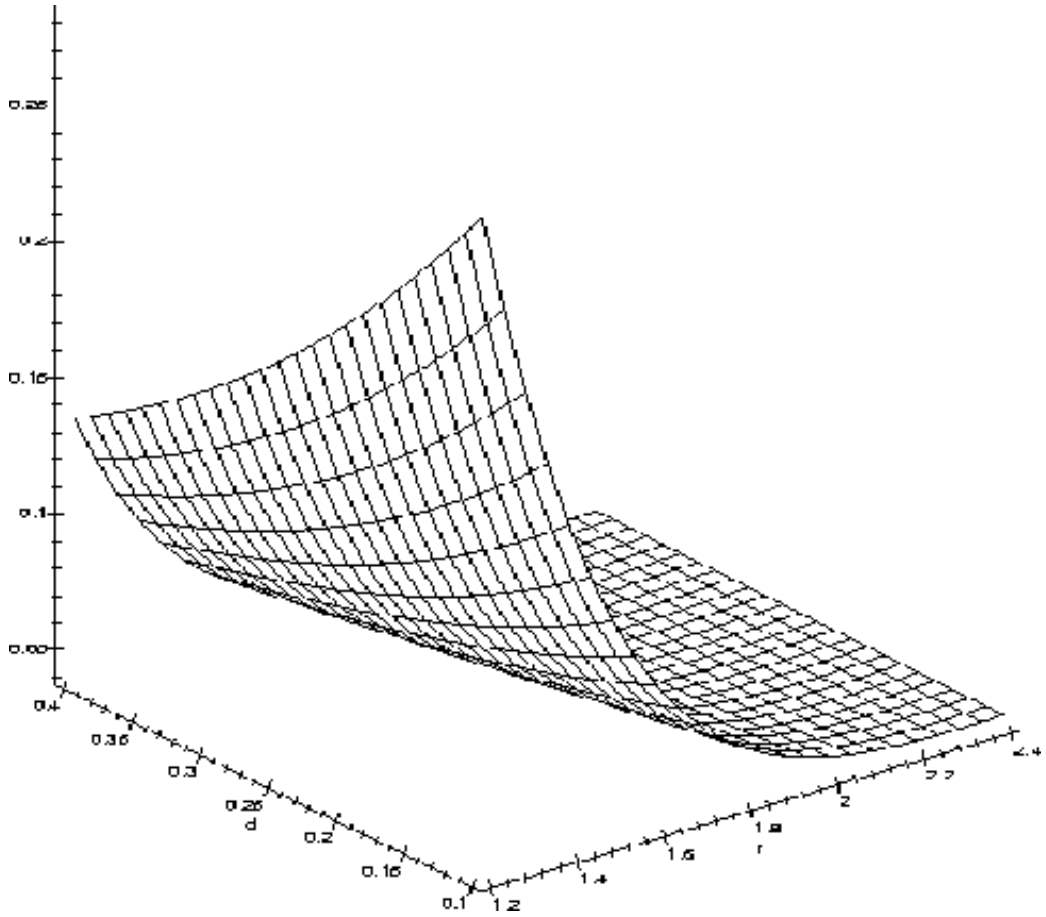

Figure 9: The μ_a-separation ability decreases with increasing distance r and d, ($n_{rel} = 1.4$, $\mu_a = 0.01[1/mm]$, $D = 0.3[mm]$).

Bibliography

[1] G. Alexandrakis, T. J. Farrell, and M. S. Patterson. Accuracy of the diffusion approximation in determining the optical properties of a two-layered medium. *Applied Optics*, **37**:7401–7410, 1998.

[2] G. Alexandrakis, T. J. Farrell, and M. S. Patterson. Monte Carlo diffusion hybrid model for photon migration in a two-layer turbid medium in the frequency domain. *Applied Optics*, **39**,13:2235–2244, 2000.

[3] R. Aronson and N. Corngold. Photon diffusion coefficient in an absorbing medium. *J. Opt. Soc. Am. A*, **16**, 5:1066–1071, 1999.

[4] S. R. Arridge and A. H. Hielscher. Personal note made at OSA conference in San Jose/CA in 1999 and Miami/FL in 2000.

[5] S. R. Arridge and W. R. B. Lionheart. Nonuniqueness in diffusion-based optical tomography. *Optics Letters*, **23**, 11:882–884, 1998.

[6] C. F. Bohren and D. R. Huffman. *Absorption and Scattering of Light by Small Particles.* Wiley, New York, 1983.

[7] A. N. Bondarenko. Structure of singularities of the fundamental solution of the transport equation. *Dokl. Akad. Nauk. SSSR*, **322**:274–276, 1992.

[8] J. T. Bruulsema, J. E. Hayward, T. J. Farrell, M. S. Patterson, L. Heinemann, M. Berger, T. Koschinsky, J. Sandahl-Christiansen, H. Orskov, M. Essenpreis, G. Schmelzeisen-Redeker, and D. Böcker. Correlation between blood glucose concentration in diabetics and noninvasively measured tissue optical scattering coefficient. *Optics Letters*, **22**, 3:190–192, 1997.

[9] K. M. Case and P. F. Zweifel. *Linear Transport Theory.* Plenum Pree, New York, 1967.

[10] S. Chandrasekhar. *Radiative Transfer.* Oxford University Press, London, 1950.

[11] M. Choulli and P. Stefanov. Inverse scattering and inverse boundary value problems for the linear Boltzmann equation. *Comm. Part. Diff. Eq.*, **21**, 5,6:763–785, 1996.

[12] P. Comon. Independent component analysis: A new concept? *Signal Processing*, **36**:287–314, 1994.

[13] D. Contini, F. Martelli, and G. Zaccanti. Photon migration through a turbid slab described by a model based on diffusion approximation. I. Theory. *Applied Optics*, **36**, 19:4587–4599, 1997.

[14] T. Cover and J. Thomas. *Elements of Information Theory.* J. Wiley and sons, New York, 1991.

[15] R. Dautray and J.-L. Lions. *Mathematical Analysis and Numerical Methods for Science and Technology*, volume 6. Springer-Verlag Berlin Heidelberg, 1993.

[16] D. J. Durian. The diffusion coefficient depends on absorption. *Optics Letters*, **23**, 19:1502–1504, 1998.

[17] T. J. Farrell, M. S. Patterson, and B. Wilson. A diffusion theory model of spatially resolved, steady-state diffuse reflectance for the noninvasive determination of tissue optical properties in vivo. *Med. Phys.*, **19**, 4:879–888, 1992.

[18] C. Führer. Finite - Elemente - Diskretisierungen der 2d - Strahlungstransportgleichung, Diplomarbeit, Universität Heidelberg, Fakultät für Mathematik, 1993.

[19] M. Girolami. *Self-organizing artificial neural networks for signal separation.* PhD thesis, Department of Computing and Information Systems, Paisley University, Scotland, 1997.

[20] S. Glasstone and M. C. Edlund. *The Elements of Nuclear Reactor Theory, Chaps. 5 and 14.* Van Nostrand, Princeton, New Jersey, 1952.

[21] R. C. Haskell, L. O. Svaasand, T.-T. Tsay, T.-C. Feng, M. S. McAdams, and B. J. Tromberg. Boundary conditions for the diffusion equation in radiative transfer. *J. Opt. Soc. Am. A*, **11**, 10:2727–2741, 1994.

[22] L. Heinemann, U. Krämer, H. M. Klötzer, M. Hein, D. Volz, M. Hermann, T. Heise, and K. Rave. Noninvasive glucose measurement by monitoring of scattering coefficient during oral glucose tolerance tests. *Diabetes Technology & Therapeutics*, **2**, 2:211–220, 2000.

[23] M. Hermann. Video-Reflectometrie zur kontinuierlichen Überwachung der optischen Eigenschaften von Haut in vivo, Diplomarbeit, Universität Heidelberg, Institut für Angewandte Physik, 1998.

[24] A. Hyvärinen. New approximations of differential entropy for independent component analysis and projection pursuit. *Advances in Neural Information Processing Systems, MIT Press*, 10:273–279, 1998.

[25] A. Hyvärinen. Survey on Independent Component Analysis. *Neural Computing Surveys*, **2**:94–128, 1999.

[26] A. Hyvärinen and E. Oja. Independent component analysis: algorithms and applications. *Neural Networks*, 13:411–430, 2000.

[27] S. L. Jacques. *Origins of tissue optical properties in the UVA, visible and NIR regions*, volume **2** of *OSA TOPS on Advances in Optical Imaging and Photon Migration*. Optical Society of America, 1996.

[28] M. Jones and R. Sibson. What is projection pursuit ? *J. of the Royal Soc.*, Series **A**, 150:1–36, 1987.

[29] C. Jutten and J. Herault. Blind separation of sources, part I: An adaptive algorithm based on neuromimetic architecture. *Signal Processing*, **24**:1–10, 1991.

[30] E. Kamke. *Differentialgleichungen, Lösungsmethoden und Lösungen*, volume 1. Akad. Verlagsges. Leipzig, 1983.

[31] G. Kanschat. Parallel and Adaptive Galerkin Methods for Radiative Transfer Problems. *Preprint 96- 29 (SFB 359)*, Universität Heidelberg, 1996.

[32] A. Kienle and M. S. Patterson. Determination of the optical properties of turbid media from a single Monte Carlo simulation. *Phys. Med. Biol.*, **41**:2221–2227, 1996.

[33] A. Kienle and M. S. Patterson. Improved solutions of the steady-state and the time-resolved diffusion equations for reflectance from a semi-infinite turbid medium. *J. Opt. Soc. Am. A*, **14**, 1:246–254, 1997.

[34] A. Kienle, M. S. Patterson, N. Dögnitz, R. Bays, G. Wagnières, and H. van den Bergh. Noninvasive determination of the optical properties of two-layered media. *Applied Optics*, **37**, 4:779–791, 1998.

[35] A. Kienle, M. S. Patterson, N. Dögnitz-Utke, R. Bays, G. Wagnières, and H. van den Bergh. Investigation of two-layered turbid media with steady-state, frequency and time domain reflectance. *Preprint*, 1997.

[36] H.-M. Klötzer. *Identifikation von Störgrößen und Entwicklung von Auswertemodellen für die nichtinvasive Glucosemessung mit optischen Sensorarrays*. PhD thesis, Technische Universität Bergakademie Freiberg, Fakultät für Chemie und Physik, 2000.

[37] M. Kohl, M. Essenpreis, and M. Cope. The influence of glucose concentration upon the transport of light in tissue-simulating phantoms. *Phys. Med. Biol.*, **40**:1267–1287, 1995.

[38] E. W. Larsen. Solution of neutron transport problems in L_1. *Comm. of Pure Appl. Math.*, **28**:729–746, 1975.

[39] T.-W. Lee, M. Girolami, A. J. Bell, and T. J. Sejnowski. A Unifying Information-theoretic Framework for Independent Component Analysis. *Int. J. on Math. and Comp. Modeling*, In press.

[40] E. E. Lewis and W. F. Miller Jr. *Computational Methods of Neutron Transport*. Wiley, New York, 1984.

[41] Q. H. Liu and Z. Q. Zhang. Nonuniform fast Hankel transform (NUFHT) algorithm. *Applied Optics*, **38**, 32:6705–6708, 1999.

[42] A. K. Louis. *Inverse und schlecht gestellte Probleme*. Teubner Stuttgart, 1989.

[43] R. E. Marshak. Note on the spherical harmonic method as applied to the Milne Problem for a sphere. *Phys. Rev.*, **71**:443–446, 1947.

[44] S. J. Matcher. Nonuniqueness in optical tomography: relevance of the P1 approximation. *Optics Letters*, **24**, 23:1729–1731, 1999.

[45] S. Nickell. Nichtinvasive Bestimmung optischer Eigenschaften der menschlichen Haut, Diplomarbeit, Universität Heidelberg, Fakultät für Physik und Astronomie, 1997.

[46] S. Nickell, M. Essenpreis, U. Krämer, M. Kohl, and D. Böcker. Determination of optical properties by variation of boundary conditions. *Preprint*, 1997.

[47] S. A. Prahl, M. Keijzer, S. L. Jacques, and A. J. Welch. A monte carlo method of light propagation in tissue. In *SPIE Institute Series*, volume IS 5, 1989.

[48] G. Schmelzeisen-Redeker. Review on Physiological and Anatomical Properties of Skin. *NIB, Part I*, Diabetes Care, DP-N, Boehringer Mannheim GmbH, 1994.

[49] W. M. Star. Comparing the P_3-Approximation with Diffusion Theory and with Monte Carlo Calculations of Light Propagation in a Slab Geometry. *SPIE Institute Series*, IS 5, 1989.

[50] W. M. Star, J. P. A. Marijnissen, and M. J. C. van Gemert. Light dosimetry in optical phantoms and in tissues: I. Multiple flux and transport theory. *Phys. Med. Biol.*, **33**, 4:437–454, 1988.

[51] W. Stoer. *Numerische Mathematik*, volume 1. Springer, 1993.

[52] G. J. Tearney and other. Determination of the refractive index of highly scattering human tissue by optical coherence tomography. *Optics Letters*, **21**:2258–2260, 1995.

[53] J.-M. Tualle, E. Tinet, J. Prat, B. Gelebart, and S. Avrillier. *Light propagation in layered media: a new analytical model for ultrafast calculation of the direct problem.* OSA Technical Digest Series, paper AMA3-1. Opt. Soc. Am., 1999.

[54] H. C. van de Hulst. *Multiple Light Scattering: Tables, Formulas and Applications.* Academic, New York, 1980.

[55] L. V. Wang. Rapid modeling of diffuse reflectance of light in turbid slabs. *J. Opt. Soc. Am. A*, **15**, 4:936–944, 1998.

[56] J. Weickert. *Anisotropic Diffusion in Image Processing.* B. G. Teubner Stuttgart, 1998.

[57] T. Weiler. P_N - Approximations for Radiative Equations and Applications to Medical Tissue Analysis, Diplomarbeit, Universität Kaiserslautern, Technomathematik, 1998.

[58] K. Yosida. *Functional Analysis.* Springer-Verlag Berlin, Heidelberg, 1995.

[59] L. Yu, M. Huan, M. Chen, W. Chen, W. Huang, and Z. Zhu. Quasi-discrete Hankel transform. *Optics Letters*, **23**, 6:409–411, 1998.